AGU PUBLICATIONS

Geochemistry, Geophysics, Geosystems

RESEARCH ARTICLE
10.1002/2016GC006588

Key Points:
- The mineralogy of fault rocks recovered in DFDP-1 is consistent for >120 km along-strike
- Authigenic phyllosilicates and carbonates occur in the Alpine Fault core
- Alpine Fault core alteration reactions alter fault zone permeability and promote interseismic strain buildup

Supporting Information:
- Supporting Information S1
- Table S1
- Table S2
- Table S3
- Data Set S1
- Data Set S2–S3

Correspondence to:
C. Boulton,
carolyn.boulton@liverpool.ac.uk

Citation:
Boulton, C., C. D. Menzies, V. G. Toy, J. Townend, and R. Sutherland (2017), Geochemical and microstructural evidence for interseismic changes in fault zone permeability and strength, Alpine Fault, New Zealand, *Geochem. Geophys. Geosyst.*, *18*, 238–265, doi:10.1002/2016GC006588.

Received 12 AUG 2016
Accepted 12 DEC 2016
Accepted article online 29 DEC 2016
Published online 25 JAN 2017

Geochemical and microstructural evidence for interseismic changes in fault zone permeability and strength, Alpine Fault, New Zealand

Carolyn Boulton[1,2], Catriona D. Menzies[3], Virginia G. Toy[4], John Townend[5], and Rupert Sutherland[5,6]

[1]Department of Geological Sciences, University of Canterbury, Christchurch, New Zealand, [2]School of Environmental Sciences, University of Liverpool, Liverpool, L69 3GP, UK, [3]Ocean and Earth Science, National Oceanography Centre Southampton, University of Southampton, Southampton, SO14 3ZH, UK, [4]Department of Geology, University of Otago, Dunedin, New Zealand, [5]School of Geography, Environment, and Earth Sciences, Victoria University of Wellington, Wellington, New Zealand, [6]GNS Science, Lower Hutt, New Zealand

Abstract Oblique dextral motion on the central Alpine Fault in the last circa 5 Ma has exhumed garnet-oligoclase facies mylonitic fault rocks from ~35 km depth. During exhumation, deformation, accompanied by fluid infiltration, has generated complex lithological variations in fault-related rocks retrieved during Deep Fault Drilling Project (DFDP-1) drilling at Gaunt Creek, South Island, New Zealand. Lithological, geochemical, and mineralogical results reveal that the fault comprises a core of highly comminuted cataclasites and fault gouges bounded by a damage zone containing cataclasites, protocataclasites, and fractured mylonites. The fault core-alteration zone extends ~20–30 m from the principal slip zone (PSZ) and is characterized by alteration of primary phases to phyllosilicate minerals. Alteration associated with distinct mineral phases occurred proximal the brittle-to-plastic transition ($T \leq 300$–$400^{\circ}C$, 6–10 km depth) and at shallow depths ($T = 20$–$150^{\circ}C$, 0–3 km depth). Within the fault core-alteration zone, fractures have been sealed by precipitation of calcite and phyllosilicates. This sealing has decreased fault normal permeability and increased rock mass competency, potentially promoting interseismic strain buildup.

1. Introduction

The Alpine Fault of New Zealand ruptures quasi-periodically in large magnitude ($M_w \sim 8$) earthquakes [*Berryman et al.*, 2012], and it represents the largest onshore seismic hazard in the country of 4.4 million people. Earthquakes are frictional instabilities, and their nucleation, propagation, and arrest are governed by fault zone properties [e.g., *Sibson*, 1977, 1982, 1992; *King*, 1986; *Wesnousky*, 1988; *Scholz*, 2002; *Ben-Zion*, 2008]. A fault zone commonly contains a fault core, often containing at least one principal slip zone (PSZ), of fine-grained and/or amorphous materials (gouge, cataclasite, or pseudotachylyte) where most coseismic displacement occurs [*Caine et al.*, 1996; *Chester and Chester*, 1998; *Sibson*, 2003]. Within the fault core, gouges, cataclasites, and breccias are interpreted to result from particle-size reduction by fragmentation, abrasion, and/or comminution accompanied by translation and rotation [e.g., *Sibson*, 1977; *Chester and Logan*, 1986; *Chester and Chester*, 1998]. Fault cores are commonly flanked by damage zones, rock bodies with micro to macroscale fractures that form as a result of off-fault deformation and fluid-rock interactions [e.g., *Chester and Logan*, 1986; *Caine et al.*, 1996].

Characterizing three-dimensional variations in fault zone properties, and taking into account time-dependent changes in these properties, is essential to understanding the physical processes that drive seismicity. As the last Alpine Fault earthquake occurred in 1717 CE and the average recurrence interval is 329 ± 68 years, current observations of the fault are ideally timed to document its late interseismic physicochemical properties [e.g., *Wells and Goff*, 2007; *Sutherland et al.*, 2007; *Howarth et al.*, 2012; *Berryman et al.*, 2012; *Townend et al.*, 2009, 2013]. The first phase of Deep Fault Drilling Project (DFDP-1) drilling in January–February 2011 retrieved a full sequence of Alpine Fault hanging wall, fault core, and footwall fault rocks, enabling detailed examination of fault zone elements on the 0.01–100 m scale [*Sutherland et al.*, 2012; *Townend et al.*, 2013; *Toy et al.*, 2015]. This study presents new field, drilling, and laboratory data on the lithology, mineralogy, and major element geochemistry of the Alpine Fault at Gaunt Creek.

2. Geological Setting

2.1. Tectonic History

The New Zealand continental landmass, Zealandia, underwent multiple phases of tectonic deformation as part of the Gondwana supercontinent [*Landis and Coombs*, 1966; *Carter and Norris*, 1976; *Mortimer*, 2004]. Zealandia was rifted during the Late Cretaceous and finally broke away from the Australia and Antarctica landmass by circa 80 Ma, with subsequent opening of the South Pacific and Tasman Sea [*Molnar et al*., 1975; *Gaina et al*., 1998; *Sutherland*, 1999]. At circa 45 Ma (Eocene), a new plate boundary propagated through Zealandia [*Sutherland*, 1995]. Strike-slip motion began on the proto-Alpine Fault circa 30 Ma [*Sutherland et al*., 2000; *Lamb et al*., 2015, 2016], and present-day oblique convergence along the Alpine Fault initiated circa 8–5 Ma as a result of a subtle shift in the location of the instantaneous Euler pole for Australian-Pacific plate motion [*Walcott*, 1984; *Batt et al*., 2004; *Cande and Stock*, 2004].

2.2. Regional Structure

The Alpine Fault is a crustal-scale transpressive fault that links Pacific Plate subduction in the north (Hikurangi margin) to Australian Plate subduction in the south (Puyseguer margin) (Figure 1). The Alpine Fault has accommodated >460 km of cumulative displacement [*Wellman*, 1953; *Lamb et al*., 2016]. The focus of this study is the Alpine Fault at Gaunt Creek, a tributary of the Waitangi-taona River on the central section of the Alpine Fault that extends for 250 km from the Toaroha River to the Martyr River. Along the central section, the fault has a strike-slip rate of 27–29 mm/yr and a dip-slip rate of 2–8 mm/yr [*Simpson et al*., 1994; *Cooper and Norris*, 1994; *Barth et al*., 2013]. In the near surface (<2 km depth), the central Alpine Fault exhibits sequences of north-northeast striking oblique thrust faults and linking east-northeast striking dextral faults, but at depth the orientation of the Alpine Fault parallels the foliation of exhumed mylonites and ultramylonites (055°/45°SE) [*Norris and Cooper*, 2007; *Barth et al*., 2012]. The structure of the central section differs

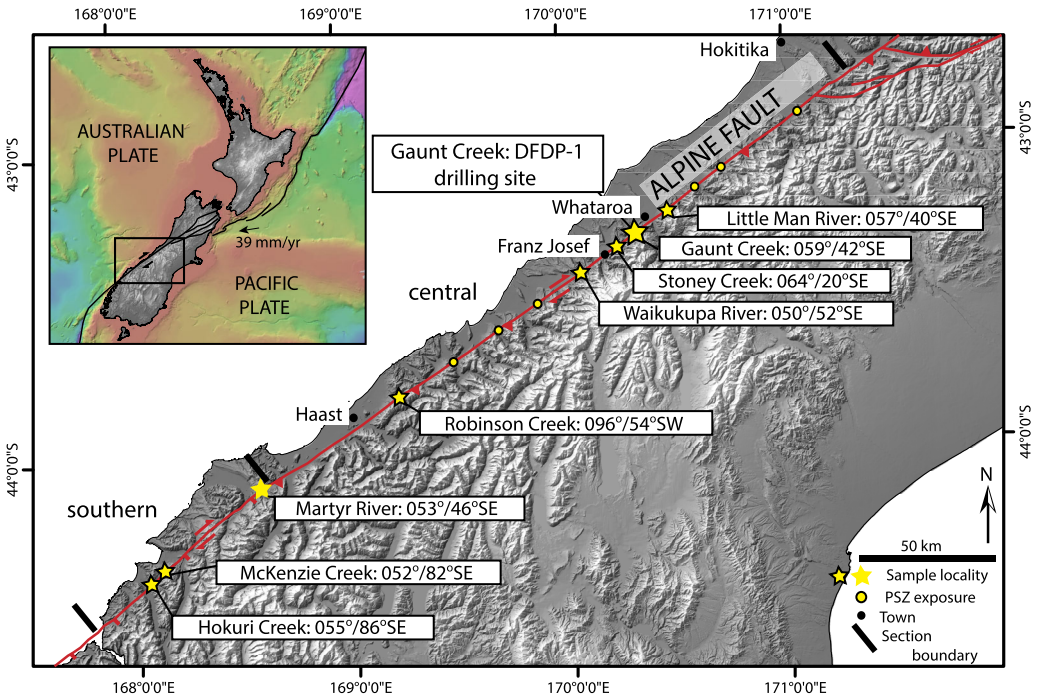

Figure 1. Location map, Alpine Fault, South Island, New Zealand. (a) The Alpine Fault forms the spine of the Southern Alps and marks the boundary between the Pacific and Australian plates. The angular velocity describing the relative motion of the Pacific and Australian plates can be resolved into ~39 mm/yr parallel to the Alpine Fault and 6–9 mm/yr perpendicular to it [*Beavan et al*., 2010]. (b) DEM image of the central South Island showing the location and strike of the Alpine Fault, which is subdivided into its central and southern sections [*Barth et al*., 2013]. Locations where fault gouge and/or cataclasite samples were collected for XRF and XRD analyses are starred in the figure (yellow star with bold outline), and fault orientation is given. At the Martyr River, only XRD analysis was conducted (yellow star). Additional exposures of thrust segment fault gouge not analyzed are shown as yellow circles; descriptions of these exposures were given by *Reed* [1964], *Wright* [1998], *Simpson* [1992], and *McClintock* [1999]. Alpine Fault cataclasites were also described by *Sibson et al*. [1979], *Simpson et al*. [1994], *Norris and Cooper* [2007], *Toy* [2007], *Easterbrook* [2010], *Toy et al*. [2011], and *Scott* [2012].

markedly from the steeply dipping oblique-normal southern Alpine Fault [see also *Berryman et al.*, 1992; *Barth et al.*, 2013] (Figure 1).

2.3. Gaunt Creek Structure

At Gaunt Creek, there are two natural exposures of the Alpine Fault basal thrust, defined by *Norris and Cooper* [2007] as the de facto plate boundary oblique thrust contact between hanging wall Pacific plate cataclasites and footwall Australian plate gravels, intrusives, or metasediments (Figure 2). One natural exposure occurs in a well-studied scarp on the south side of Gaunt Creek [*Cooper and Norris*, 1994; *Boulton et al.*, 2012], and the other is a terrace on the north side of Gaunt Creek [*De Pascale and Langridge*, 2012; *Boulton et al.*, 2012] (Figures 2 and 3). Hanging wall cataclasites and mylonites derived from metabasic and quartzofeldspathic schist protoliths outcrop in both localities [e.g., *Cooper and Norris*, 1994]. The basal thrust at Gaunt Creek has changed from a moderately southeast-dipping, oblique reverse fault to a shallowly dipping thrust that has accommodated over 180 m of overthrusting [*Cooper and Norris*, 1994]. The basal thrust exposed in the scarp on the south side of Gaunt Creek has a mean orientation of 059°/42°SE with mean slickenline striations oriented 24/086. The fault plane exposed in the terrace on the north side of Gaunt Creek is more shallowly dipping, with an average orientation of 005°/28°SE (Figure 2). No slickenline striations were found along the contact between the terrace fault gouge and footwall gravel contact. Drillcore retrieved during DFDP-1A and 1B was not oriented, and estimates of fault dip based on basal gouge contacts have an estimated margin of error of ±5°. The fault plane in DFDP-1A dips approximately 25–35°, and the primary fault plane in DFDP-1B dips approximately 45–55° (see also Figure 2 caption) [*Sutherland et al.*, 2012].

3. Methods

3.1. Drilling Operation

In Phase 1 of drilling, January and February 2011, the DFDP project completed two vertical boreholes at Gaunt Creek. DFDP-1A drilled to 100.6 m depth and DFDP-1B drilled to 151.4 m depth [*Sutherland et al.*, 2012] (Figure 3). Hanging wall, fault core, and footwall sections of fault-related rocks were recovered,

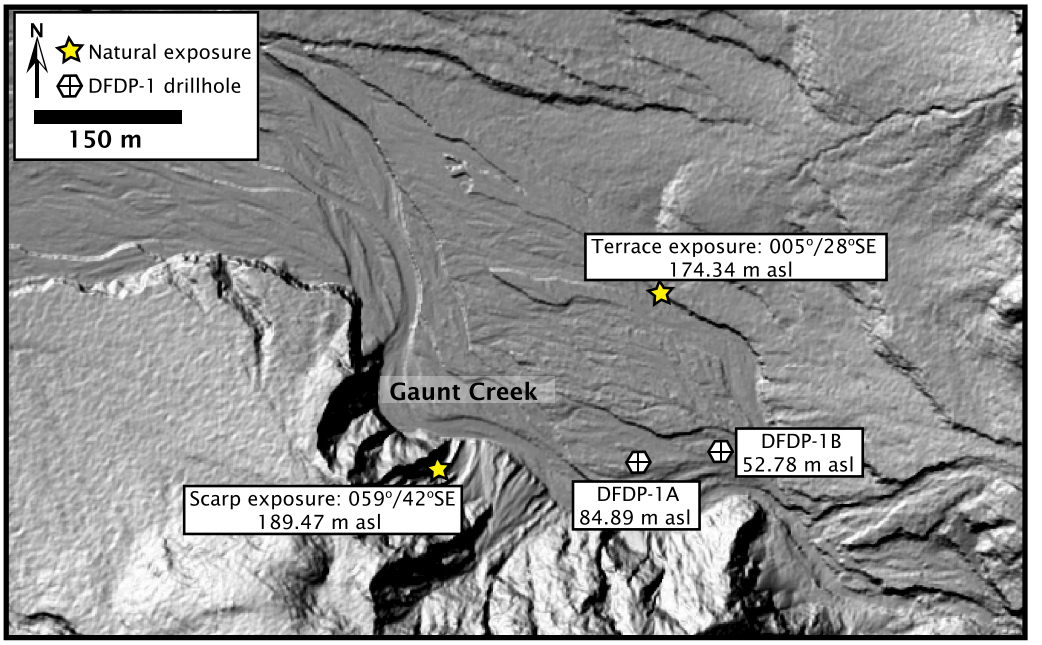

Figure 2. Hillshade view of the Gaunt Creek catchment derived from LiDAR data. The location of natural exposures of the faulted contact between (primarily) Pacific-plate-derived cataclasites and Australian-plate-derived cataclasites are shown with stars and the location of DFDP-1 drillholes is shown with crossed hexagons. Elevation of the contact is given in meters above seal level (asl). The Gaunt Creek catchment lies at the junction between dextral thrust and thrust segments of the fault [*Barth et al.*, 2012], and the strike of the fault changes from southwest to northeast across the creek. A 4 point solution constructed using the strike between the scarp and terrace exposures and the contact elevations yields an average fault dip of 28–30°.

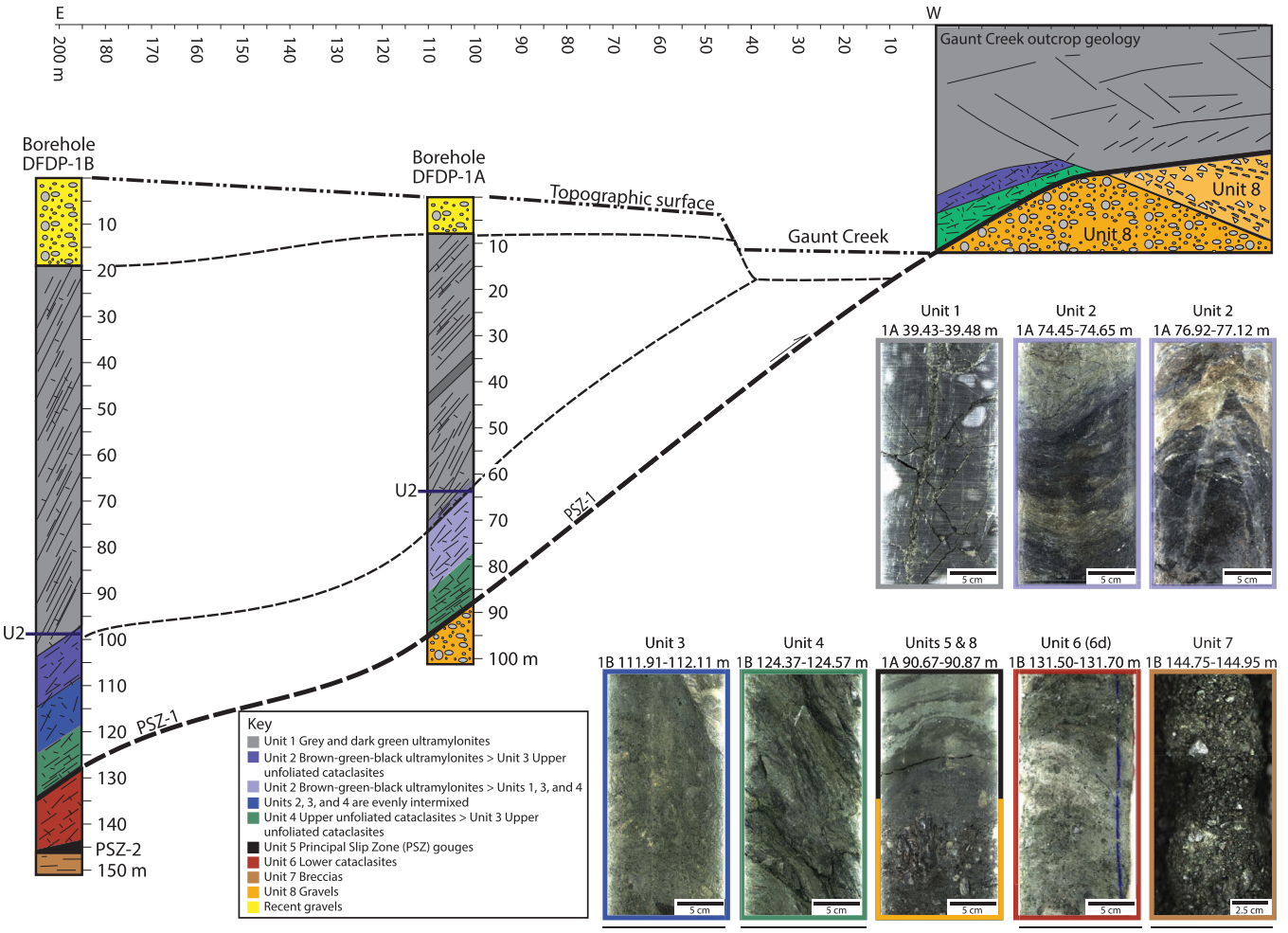

Figure 3. Schematic cross sections of fault-related rocks comprising the DFDP-1A and DFDP-1B boreholes at Gaunt Creek with reference to outcrop geology. U2 denotes the uppermost documented occurrence of altered Unit 2 brown-green-black ultramylonites in each borehole. Colors on the cross section indicate the relative proportions of each lithological unit recovered in the cored interval (see Key). Also pictured are core-scale examples of major lithological units identified in DFDP-1A and DFDP-1B. Each picture is a 180° core scan, except for 1B 144.75-144.95 m, which is a flat core scan. Colored boxes around each core-scale image correspond to the borehole depth interval from which they were sampled. Figure modified from *Sutherland et al*. [2012] and *Toy et al*. [2015].

wireline logs were completed, hydraulic observations were made, and downhole observatories for the long-term monitoring of temperatures, fluid pressures, and seismicity were established. Drilling methods are described elsewhere in the detailed operational report [*Sutherland et al*., 2011].

3.2. Core Logging

Detailed core logs were made of 148 m of near-complete whole-rock cores (PQ, 85 mm-diameter). Initial geological logs completed on site recorded lithology, color, distribution, styles, and orientations of meso to microscale structures. More detailed imaging, logging, and lithological descriptions of the core were conducted after transport to the University of Otago (for core-logging methods, see *Sutherland et al*. [2011]).

3.3. Thin Section Preparation

Representative samples of fault-related rocks were selected and made into petrographic thin sections. Petrographic thin sections of fragile fault gouges and cataclasites were prepared dry and polished using 1 μm diamond paste. Less friable drillcore materials were prepared using standard petrographic thin section making techniques.

3.4. Analytical Methods

Qualitative X-ray diffraction (XRD) analyses were conducted on 34 clean samples collected from DFDP-1A and DFDP-1B drillcore. Qualitative XRD measurements were performed on a PANalytical X'Pert PRO MPD

PW 3040/60 X-ray diffractometer in the Department of Geology, University of Otago. Measurement conditions were 40 kV, 30 mA, CuK_α radiation with 0.125° divergence slit size. XRD patterns were recorded in steps of 0.0080°2θ using X'Pert Data Collector version 2.0e and processed with X'Pert HighScore version 2.2b.

Quantitative XRD analyses were conducted on six fault gouges and cataclasites in DFDP-1B at CSIRO Land and Water, Urrbrae, Austrlia. XRD patterns were recorded in steps of 0.017°2θ on a PANalytical X'Pert Pro Multipurpose Diffractometer using Fe-filtered Co Kα radiation, variable divergence slit, 1° antiscatter slit and fast X'Celerator Si strip detector. Quantitative analysis was performed using SIROQUANT, a commercially available software package from Sietronics Pty Ltd. To document along-strike variations in the mineralogy of principal slip zone gouges and cataclasites, 17 additional quantitative whole rock XRD analyses were conducted on surface-outcrop fault gouges and cataclasites collected from localities pictured in Figure 1.

A subset of DFDP-1 samples, together with fault core samples from natural exposures at Gaunt Creek, were analyzed for major element geochemistry using Inductively Coupled Plasma Atomic Emission Spectroscopy (ICP-AES) and X-ray fluorescence (XRF) techniques. Thirty-nine clean samples from DFDP-1A and DFDP-1B, weighing between 10 and 30 g, were selected for ICP-AES analysis by ALS Minerals, ALS Canada Ltd., North Vancouver, British Columbia, Canada. Major element oxide analysis of six DFDP-1A samples was performed using XRF at the Department of Geology, University of Otago, using a Philips PW2400 X-ray fluorescence spectrometer.

To determine loss on ignition (LOI), 1.0 g of prepared sample was placed in an oven at 1000°C for 1 h, cooled, and then reweighed by ALS Minerals. At the Department of Geology, University of Otago, 2.0 g of rock powder was placed in an oven at 1100°C for 2 h, cooled, and then reweighed. The percentage loss on ignition is reported as the percentage difference in sample weight.

To constrain the along-strike applicability of DFDP-1 results, 23 additional major element analyses were conducted on ultramylonite (1), hanging wall cataclasites (8), fault core gouges (12), and footwall gravel cataclasites (2) using a combination of the above methods. Sample collection localities span 234 km along-strike of the Alpine Fault and are indicated in Figure 1. A detailed analysis of along-strike variations in fault gouge, cataclasite, and footwall gravel major element geochemistry is outside the scope of this research, and the following results, discussion, and conclusions sections focus on DFDP-1 samples. Tabulated results for other localities along strike can be found in supporting information along with reports on analytical error and detailed qualitative and quantitative XRD, ICP-AES, and XRF methods (see also Table 4 caption) (supporting information S1–S3).

4. Results

4.1. Fault Zone Structure

Four main fault-rock units were initially identified in the DFDP-1 boreholes: hanging wall ultramylonite, hanging wall cataclasite, principal slip zone fault gouge (PSZ), and footwall cataclasite [*Sutherland et al*., 2012]. Within DFDP-1B, two PSZ gouges were identified: one between hanging wall cataclasite and the footwall cataclasite (PSZ-1), and another within footwall cataclasites (PSZ-2) (Figure 3). Within 50 m of the PSZ, clay-filled zones were identified, and enhanced calcite and phyllosilicate mineralization was found within ~20 m of the PSZ [*Sutherland et al*., 2012]. The PSZ fault gouge that marks the boundary between hanging wall cataclasites and footwall gravel was intercepted at 90.5 m depth in DFDP-1A. The PSZ-1 fault gouge that marks the boundary between hanging wall cataclasites and footwall granitoid or metasediment-derived cataclasites was intercepted at 128.3 m in DFDP-1B (DFDP-1B depths given here are corrected by +0.20 m following *Townend et al*. [2013]). Permeability decreases through the cataclasites and reaches a minimum at the PSZ fault gouges, but hanging wall mylonites are highly permeable [*Sutherland et al*., 2012; *Carpenter et al*., 2014].

4.2. Lithologic Units

Using detailed imaging, core logging, lithological descriptions, and thin section analysis, a refined model of hanging wall, fault core, and footwall lithologic units has been developed [*Townend et al*., 2013; *Toy et al*., 2015] (Figure 3 and Table 1). Fault rocks were described following the scheme proposed by *Sibson* [1977] and modified to include the presence of foliated cataclasites with an interconnected network of

Table 1. Description of Lithologic Units Recovered in DFDP-1 Modified From *Toy et al.* [2015][a]

Lithologic Unit	Name	Description	Dominant Microstructure(s)	Grain Size (mm)	Mineralogy
Unit 1	Grey and dark green ultramylonites	Planar-foliated mylonite to ultramylonite	Segregations of Qtz+Pl and Ms+Bt± Ep±Chl with locally abundant Pl-augen trains, mm-spaced continous foliation	>0.03–>1	Qtz+Pl+Bt+Ms±Cal±Am±Ep±Cl±Ilm±Ttn
Unit 2	Brown-green-black ultramylonites	Planar-foliated ultramylonite	Indistinct mm-spaced foliation defined by opaque seams and parallel mica grains which form a locally dilatant disjunctive cleavage; Pl-augen common	<0.05–<0.2	Qtz+Pl+Bt+Ms+Cl±Cal±Ep±Am±Ilm±Ttn
Unit 3	Upper unfoliated cataclasites	Unfoliated cataclasites derived from Units 1 and 2	Angular clasts of Units 1 and 2 in a variably calcite-cemented ultrafine-grained matrix (<0.1 mm-grains)	<0.01–<0.1 with <100 clasts	Qtz+Pl+Bt+Ms+Cl±Cal±Ep±Am±Ilm±Ttn
Unit 4	Upper foliated cataclasites	Foliated cataclasites derived from Units 1-3	Foliation defined by micro-shears, anastamosing seams of opaques, and/or locally aligned phyllosilicates; e-twinned veins and clasts of calcite	<0.01–<0.1	Qtz+Pl+Ms+Cl+Cal±Bt±Ep±Am±Ilm±Ttn
Unit 5	Gouges	Cemented to uncemented gouges with variable mineralogy	Predominantly random fabric with rare locally aligned phyllosilicates; e-twinned calcite clasts; gouge and cataclasite clasts common	<0.001–<0.01	Qtz+Pl+Ms+Cl+Cal±Ksp±Sme(Mnt)± Kln±Gt±Mn±Ilm±Ttn±Zrn±Ap
Unit 6	Lower cataclasites-divided into 4 subunits	6a- white to cream-colored ccl with granitoid and gneissic clasts; 6b- greenish grey foliated protocataclasite; 6c- greenish grey to black ultracataclasite to gouge with gneiss, Qtz-Pl-Fsp, and rare mylonite clasts; 6d- a mixture of 6a-6c.	6a- random fabric, granitoid clasts contain myrmekite and antiperthite textures, gneissic clasts contain ribbon Qtz; 6b—foliations comprise muscovite and chlorite; 6c- random fabric; 6d - interlayered mixture of 6a-6c containing numerous micro to meso-scale faults	≪0.03–≫0.1	Qtz+Ksp+Pl+Ms±Bt±Cl±Zrn±Ap±Ttn
Unit 7	Breccias	Protoccl to breccia composed of black myl-gneiss clasts	Remnant mylonitic-gneissic foliation with Pl-augen or Qtz segregations; phyllosilicate foliations wrap porphyroclasts	<1–>10	Qtz+Ksp+Pl+Ms+Bt+Cl+Ep+Ap+Ttn+Gr
Unit 8	Gravels	Quaternary gravels composed primarily of Alpine Schist clasts	Locally imbricated	0.25–>10	Qtz+Pl+Bt+Ms±Cal±Am±Ep±Cl±Ilm±Ttn

[a]Grain size describes matrix grains and clasts and/or porphyroclasts. Abbreviations are: Qtz is quartz, Pl is plagioclase (primarily oligoclase and/or albite), Bt is biotite, Ms is muscovite, Cal is calcite, Am is amphibole, Ep is epidote, Cl is chlorite, Ilm is ilmenite, Ttn is titanite, Sme is smectite, Mnt is montmorillonite, Kln is kaolinite, Gt is goethite, Mn is manganese oxide-hydroxide, Zrn is zircon, Ap is apatite, and Gr is graphite.

phyllosilicate minerals [*Chester et al.*, 1993; *Jefferies et al.*, 2006]. Summaries of these lithologic units have been modified from *Toy et al.* [2015] and are outlined in Table 1.

Core-scale examples of each lithologic unit are given in Figure 3. Details are given in the caption. Figure 4 depicts plane-polarized optical microscopy (OM) images of the Units 2–3 transition (Figure 4a), Unit 4 (Figures 4b–4d), Unit 5 (Figure 4g), Unit 6 (Figures 4e and 4f), and Unit 7 (Figure 4h). In Figures 5 and 6, scanning-electron microscope backscattered electron (BSE) images reveal the finer-scale details of compositional variations and microstructural features in lithologic units: 2 (Figures 5a and 5b); 3 (Figures 5c and 5d); 4 (Figures 5e and 5f); 5 (Figures 6a–6d); 6 (Figures 5h and 6e–6g); and 7 (Figure 6h).

4.3. Mineralogy

X-ray diffraction analyses provide an indication of the minerals present in abundances greater than ~5%. All the samples analyzed contain quartz, plagioclase, white mica (muscovite and/or illite), and chlorite (clinochlore). Carbonate minerals (calcite + ankerite) are most prevalent in hanging wall samples (Units 1–5) and are only sporadically present in Units 6 and 7 beneath the 128.3–128.5 m PSZ in DFDP-1B. Potassium feldspar (K-feldspar) is only found in the hanging wall within 5 m of the PSZ in DFDP-1A and, primarily, beneath PSZ-1 in DFDP-1B (Table 2).

Six whole-rock samples from the DFDP-1B principal slip zone intervals (PSZ-1 and PSZ-2) were analyzed for quantitative XRD analysis. The modal abundance of phyllosilicates in Units 5 (PSZ-1, 128.3 m; PSZ-2,

144.02 m; PSZ-2, 144.14 m depth), Unit 6 (143.9 m depth), and Unit 7 (144.28 m depth) does not vary significantly, being 35–36% for Units 5 and 6, and 27% for Unit 7. The primary difference between the samples lies in the presence of dioctahedral smectite (montmorillonite) in the Unit 5 brown gouges (Table 3).

Whereas nonfoliated and foliated cataclasites in the hanging wall and footwall contain the phyllosilicates chlorite and white mica, Unit 5 fault core gouges in the DFDP-1 boreholes contain kaolinite, dioctahedral

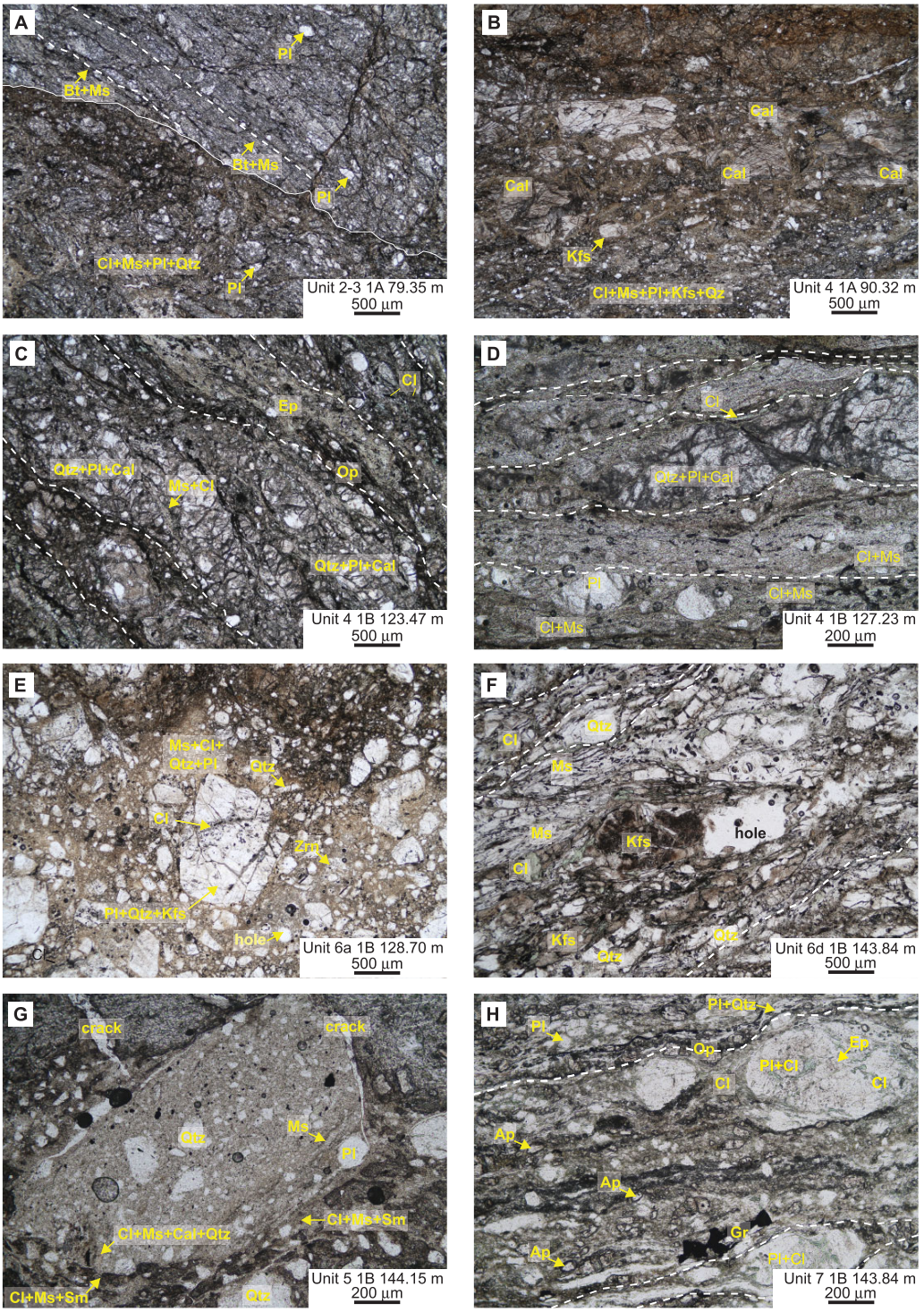

Figure 4.

smectite (montmorillonite), white mica, and rare chlorite (Tables (1–3)). Standard X-ray diffraction techniques are unable to distinguish the white micas muscovite and illite, but the distinction is important because illite is a low-temperature authigenic phyllosilicate indicative of retrograde alteration concomitant with exhumation. Clay mineral polytype analyses on DFDP-1B clay separates recently revealed that high proportions of $1M_d$ authigenic illite (80–95%) occur only within the PSZ gouges [*Schleicher et al*., 2015]. These results suggest that additional alteration reactions resulting in the formation of low temperature phyllosilicates are occurring preferentially in the Unit 5 gouges.

Montmorillonite-bearing Unit 5 gouges were also found on basal thrusts on a tributary of Little Man River, Waikukupa River, and Robinson Creek, an along-strike distance of 120 km on the central Alpine Fault (Figure 1 and Table 4). On the southern Alpine Fault, PSZ gouges contain saponite and serpentine and have been derived partly from ultramafic protoliths (Figure 1 and Table 4) [*Barth et al*., 2013].

4.4. Major Element Geochemistry

Major element geochemistry and LOI results for DFDP-1A fault rocks are presented in Table 5; results for DFDP-1B fault rocks are presented in Table 6. The DFDP-1A borehole sampled hanging wall fault rocks, a single PSZ, and footwall gravels. DFDP-1B borehole samples span the hanging wall and footwall and include two PSZ intervals (Figure 3). Major element data show a clear distinction between the SiO_2, Al_2O_3, CaO, and K_2O contents of the Units 2–4 and Unit 6 fault rocks; Unit 5 gouges are distinguished by high CaO and LOI values (Figures 7 and 8). SiO_2 concentrations in hanging wall and footwall rocks overlap, but Unit 6 lower cataclasites between 128.04 and 128.22 m depth, and at 131.68 m depth, have the highest SiO_2 contents (70.70–74.60 wt.%, Figure 8). Unit 6 lower cataclasites between 138.17 and 141.07 m also contain relatively higher amounts of Al_2O_3 (16.65–18.10 wt.%, Figure 8).

In DFDP-1A, the highest CaO concentrations occur in the Unit 4 upper foliated cataclasite (90.32 m depth) and Unit 5 gouge (90.62 m depth) (14.75 and 6.83 wt.%, respectively) (Figure 7). In DFDP-1B, all Unit 3–5 fault rocks, with the exception of a Unit 5 gouge at 144.15 m depth, have higher CaO concentrations (2.79–6.72 wt.%) than the Unit 6 lower cataclasites (0.58–2.58 wt.%). The Unit 8 footwall gravel in DFDP-1A (91.3 m depth) records the lowest CaO content (1.36 wt.%). Overall, Unit 6 lower cataclasites have mean higher K_2O (4.28 ± 1.14 wt.%, $n = 13$) concentrations than other footwall and hanging wall units (3.19 ± 0.57 wt.%, $n = 26$) (Figures 7 and 8). Na_2O shows less discernible trends but usually occurs more abundantly in the Unit 6 lower cataclasites (Figure 8).

All Unit 5 gouges, the Unit 4 foliated cataclasite at 90.32 m depth in DFDP-1A, and the Unit 3 upper unfoliated cataclasite at 116.72 m depth in DFDP-1B have elevated MnO contents (0.11–0.24 wt.%), particularly when compared to the Unit 6 cataclasites (0.01–0.08 wt.%, Figures 7 and 8). Unit 6 lower cataclasites immediately below PSZ-1 contain relatively less Fe_2O_3 and MgO (1.31–2.92 wt.% and 0.59–1.39 wt.%, respectively), but considerable scatter exists within the hanging wall and footwall units. The Unit 7 breccia at 146.25 m depth has the highest concentration of P_2O_5 (0.44 wt.%) (Figure 8; see also Figure 4h). In both DFDP-1A and DFDP-1B, the Unit 5 gouges and adjacent Unit 4 upper foliated cataclasites have high LOI and CaO values (Figures 7 and 8).

Major element oxide data are presented on two ternary plots in Figure 9. Together with Pacific Plate quartzofeldspathic schist and metabasite, the Australian Plate Karamea Suite and Greenland Group protoliths define a trend line along which the majority of DFDP-1 hanging wall and footwall fault rocks lie (Figure 9a). The Unit 7 breccia lies at the $MgO + Fe_2O_3$ axis of the footwall trend line in both ternary plots (Figure 9).

Figure 4. Plane-polarized light (PPL) optical microscope (OM) images of representative DFDP-1 fault rock lithologic units. Borehole depths are given on each image. 1A indicates DFDP-1A and 1B indicates DFDP-1B. (a) Unit 2 brown-green-black ultramylonite. In this OM image, the disjunctive cleavage spacing is < 1 mm and defined by fine-grained phyllosilicates and opaques (dashed white lines). Unit 2 is commonly interlayered with Unit 3 and a typical contact is shown (solid white line). (b) Abundant e-twinned calcite in a Unit 4 foliated cataclasite. A planar foliation appears at the bottom of the images, and it is defined by fine-grained opaques, chlorite, muscovite, plagioclase, potassium feldspar, and quartz. (c) Unit 4 foliated cataclasite with boudinaged porphyroclasts of quartz, plagioclase, and calcite. Chlorite commonly occurs in zones of dilatation. Opaques, muscovite, chlorite, and rare epidote, form the foliation (dashed white lines). (d) Unit 4 foliated cataclasite with anastomosing foliation defined by chlorite and muscovite with accessory graphite (dashed white lines). (e) Unit 6a lower cataclasite derived from a granitoid protolith. Intragranular fracture in center clast is filled with chlorite; matrix is composed of ultrafine-grained chlorite, muscovite, quartz, and plagioclase. (f) Unit 6d lower cataclasite with an anastomosing foliation of ribbon quartz and muscovite grains derived from a gneissic protolith (cf., Figure 6f) (dashed white lines). (g) Gouge clast in lower DFDP-1B Unit 5 gouge. Note concentration of phyllosilicates along margins of gouge clast (arrows). (h) Unit 7 breccia clasts have a mylonitic foliation (dashed white lines) defined by opaques and elongated plagioclase and quartz; accessory graphite and apatite are also common.

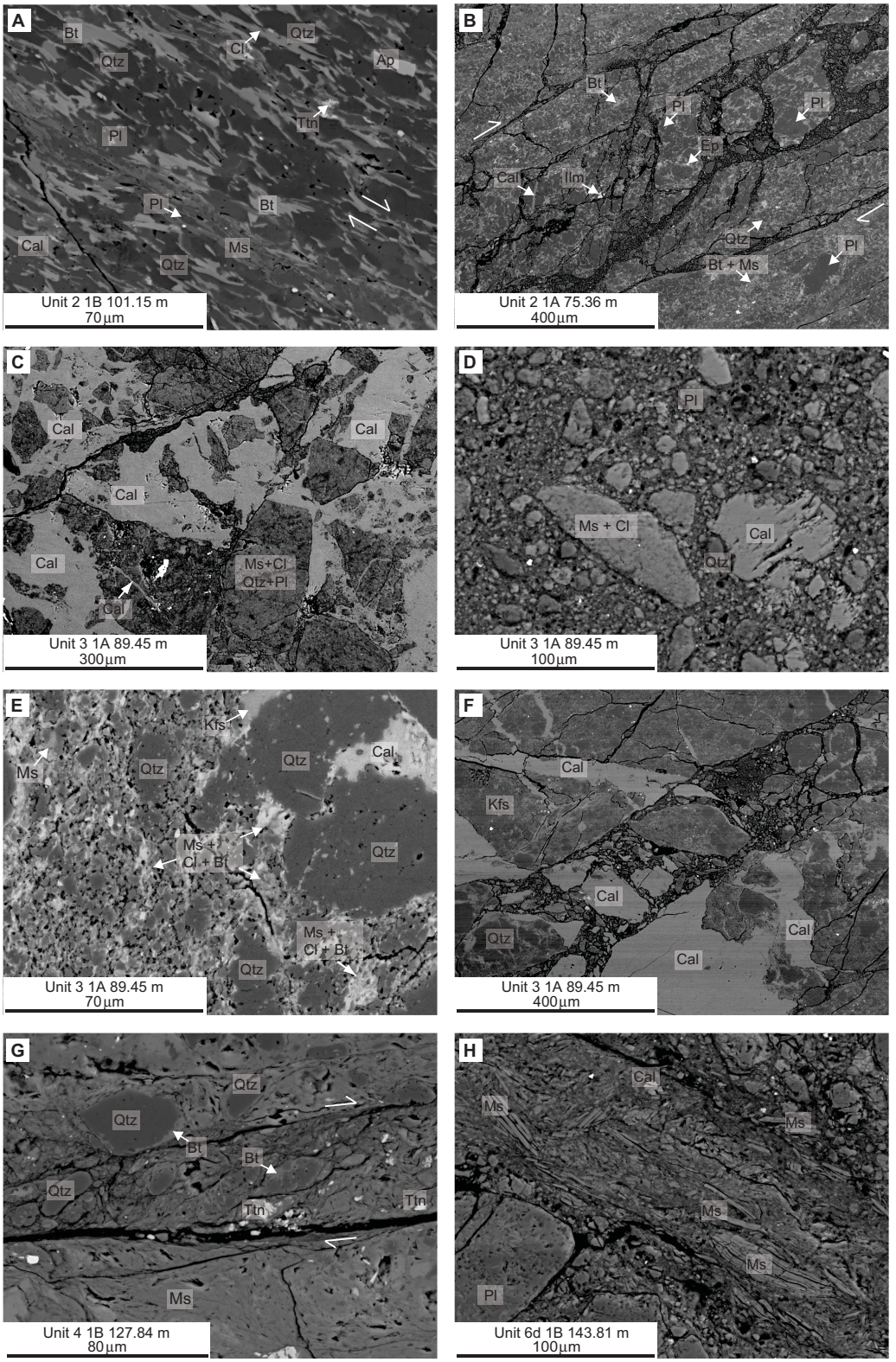
A
Bt
Qtz
Cl
Qtz
Ap
Ttn
Pl
Pl
Bt
Cal
Ms
Qtz
Unit 2 1B 101.15 m
70 µm
B
Bt
Pl
Pl
Ep
Cal
Ilm
Qtz
Pl
Bt + Ms
Unit 2 1A 75.36 m
400 µm
C
Cal
Cal
Cal
Cal
Ms+Cl
Qtz+Pl
Cal
Unit 3 1A 89.45 m
300 µm
D
Pl
Ms + Cl
Cal
Qtz
Unit 3 1A 89.45 m
100 µm
E
Kfs
Ms
Qtz
Qtz
Cal
Ms +
Cl + Bt
Qtz
Ms +
Cl + Bt
Qtz
Unit 3 1A 89.45 m
70 µm
F
Cal
Kfs
Cal
Qtz
Cal
Cal
Unit 3 1A 89.45 m
400 µm
G
Qtz
Qtz
Bt
Bt
Qtz
Ttn
Ttn
Ms
Unit 4 1B 127.84 m
80 µm
H
Cal
Ms
Ms
Ms
Ms
Pl
Unit 6d 1B 143.81 m
100 µm

Figure 5.

Unit 6 lower cataclasites have higher K_2O, Na_2O, and Al_2O_3 compared with the other units and trend towards the average Karamea Suite protolith composition (Figure 9a). A trend towards higher CaO is exhibited by Unit 4 upper foliated cataclasites and Unit 5 gouges, with the DFDP-1B PSZ-2 gouge (144.15 m depth) having lower CaO than the DFDP-1B PSZ-1 gouge and DFDP-1A PSZ gouge (Figure 9b).

5. Discussion

5.1. Alteration Zone Processes

During exhumation from ~35 km depth, brittle deformation of Alpine Fault mylonites, accompanied by fluid infiltration, has resulted in complex mineralogical and lithological variations in fault rocks retrieved during DFDP-1 drilling at Gaunt Creek. Results documented herein and referred to in publications by *Sutherland et al*. [2012], *Townend et al*. [2013], and *Toy et al*. [2015] reveal that the fault comprises a fault core of protocataclasites, cataclasites, and fault gouges bounded by a damage zone containing fractured ultramylonites (Figure 3). These results are consistent with previous descriptions of Alpine Fault rocks [e.g., *Reed*, 1964; *Sibson et al*., 1979; *Norris and Cooper*, 2007; *Toy et al*., 2008]. In the DFDP-1 drillcore, the fault core-alteration zone extends from the Unit 5 PSZ gouges ~20–30 m into the hanging wall by using the first documented occurrence of retrogressed mineral assemblages in the Unit 2 brown-green-black ultramylonites to represent the maximum width of alteration zone processes [e.g., *Caine et al*., 1996; *Sutherland et al*., 2012]. Measurements made from fault rocks collected elsewhere on the central and southern Alpine Fault reveal that fault core mineralogy at the site of DFDP-1, Gaunt Creek, is similar to outcrops exposed for at least 120 km along-strike (Figure 1) (Tables 3 and 4). We combine our observations with the temperature constraints of *Warr and Cox* [2001] and *Toy et al*. [2010] and the reactions documented by *Chamberlain et al*. [1999] and *Wintsch and Yeh* [2013] to suggest that at least two stages of chemical alteration have occurred in the Alpine Fault core-alteration zone (Figure 10). At temperatures at or near the brittle-to-ductile transition ($T \leq 300$–$400°C$), metasomatic alteration reactions resulted in albite or, potentially, K-feldspar replacement by muscovite, and biotite (phlogopite) replacement by chlorite (clinochlore). Hydrous chloritization of epidote and hornblende (actinolite) may have also occurred (Figures 4c 5d, and 5e). Given its ubiquitous presence in alteration zone lithological units including ultramylonites (Figure 5a), chlorite likely precipitated at a range of temperatures less than 400°C, temperature conditions slightly broader than those defined by *Warr and Cox* [2001] using microchemical data [see also *Vry et al*., 2001]. At lower temperatures ($T \leq 120°C$), alteration reactions occurred in the presence or absence of free electrons. That is, depending on local redox conditions, primary minerals were altered to kaolinite, smectite (montmorillonite), and/or pyrite or smectite (montmorillonite), kaolinite, Fe-hydroxide (goethite), and/or carbonate (Tables 3 and 4, Figures 4g, 6a, 6b, and 10).

For the standard metasomatic alteration reactions involving K-feldspar, plagioclase, muscovite, biotite (phlogopite), and chlorite (clinochlore), volume loss or gain, and corresponding variations in porosity and permeability, are governed by fluid:rock ratios and Mg^{2+}/H^+, K^+/H^+, and Na^+/H^+ activity ratios [*Wintsch et al*., 1995; *Wintsch and Yeh*, 2013]. Hydrolysis reactions involving the reactants K-feldspar, muscovite, biotite (phlogopite), muscovite, chlorite (clinochlore), and albite usually result in volume loss. Notably, however, a volume gain occurs during the alteration of clinochlore to montmorillonite and during the alteration of muscovite to illite. Precipitation of calcite and goethite also results in a volume gain of 36.9 cm^3 per mol of

Figure 5. Scanning electron microscope (SEM) backscattered electron (BSE) images of representative DFDP-1 fault rock lithologic units. All thin-sections are not oriented. Borehole depths are given on each image. 1A indicates DFDP-1A and 1B indicates DFDP-1B. For all microstructures: Qtz is quartz; KSp is potassium feldspar; Pl is plagioclase; Ms is muscovite; Cl is chlorite; Bt is biotite; Sm is smectite; Cal is calcite; Op is opaques; Ilm is ilmenite; Ttn is titanite; Ep is epidote; and Zrn is zircon. (a) Unit 2 brown-green-black ultramylonite. A ~mm-spaced disjunctive cleavage appears as fine-grained, parallel grains of plagioclase (oligoclase) and muscovite with accessory titanite. Shear sense given by stair-stepped quartz clast. (b) Unit 2 brown-green-black ultramylonite with an anastomosing network of cataclasite-filled fractures, which yield a shear sense. (c) Unit 3 upper unfoliated cataclasite composed of angular clasts of altered Unit 2 cemented with calcite (similar to the mosaic breccia of *Woodcock and Mort* [2008]). (d) Typical Unit 3 upper unfoliated cataclasite random-fabric matrix composed of altered plagioclase porphyroclasts, quartz, and calcite with embayed margins. (e) Unit 4 upper foliated cataclasite which has a Unit 2 protolith identical to image (a). Note strongly corroded clast margins, enhanced porosity, and ultrafine-grained matrix chlorite and muscovite. (f) Unit 4 upper foliated cataclasite with foliation defined by comminuted grains. Protolith appears similar to Unit 2 in image (a), but alteration to chlorite and white mica is ubiquitous. Note also the presence of potassium feldspar, which is not present in Unit 2. (g) Unit 4 upper foliated cataclasite with foliation defined by aligned phyllosilicates that appear to link in an anastomosing network similar to an S-C″ shear fabric. (h) A foliated portion of a Unit 6d lower cataclasite. The foliation is defined by ~100 μm-long aligned muscovite grains sourced from a gneissic protolith. Calcite is sparse.

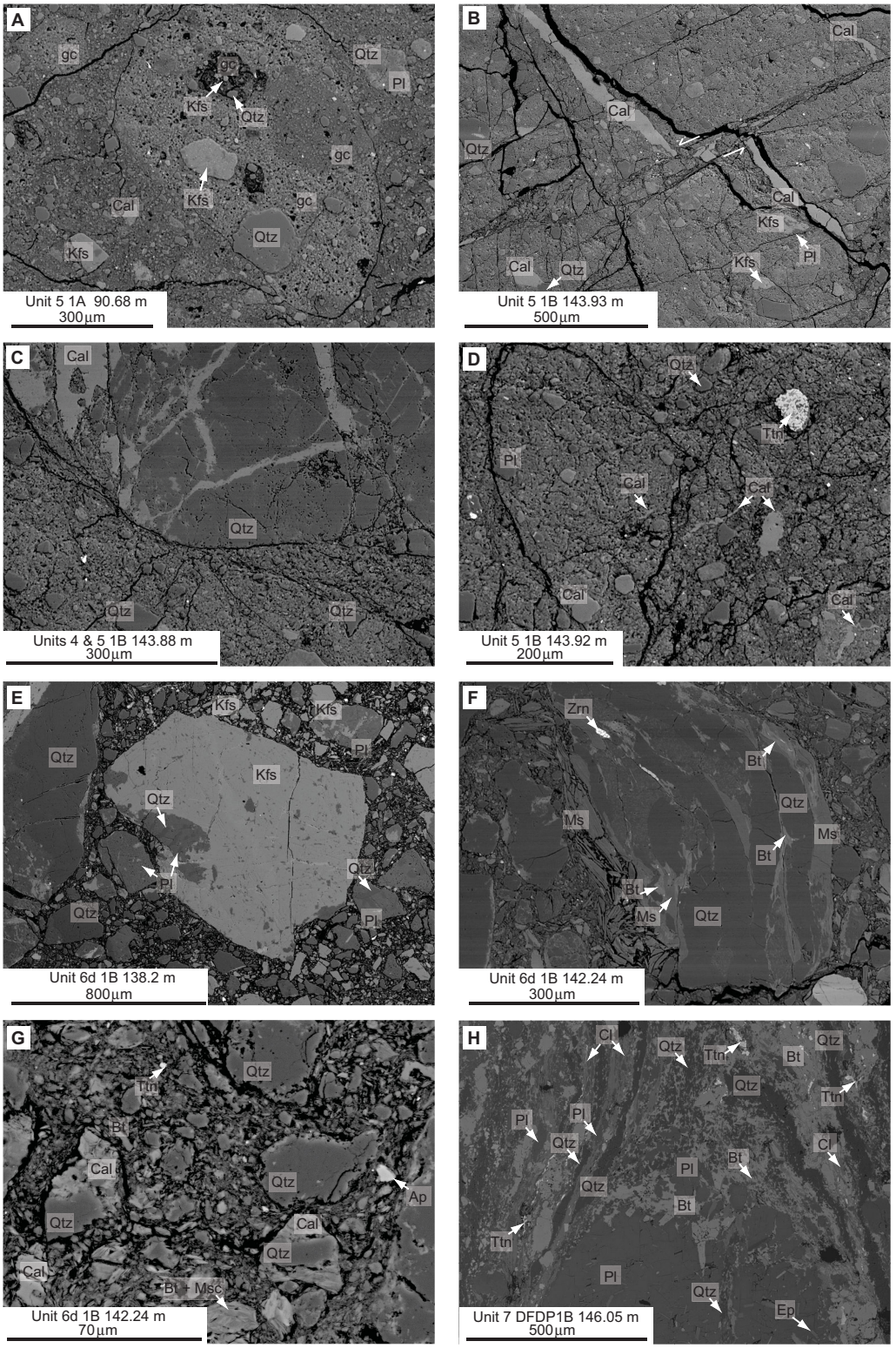
A
gc
Qtz
Pl
Kfs
Qtz
gc
Kfs
Cal
gc
Qtz
Kfs
Unit 5 1A 90.68 m
300µm
B
Cal
Cal
Qtz
Cal
Kfs
Cal
Qtz
Kfs
Pl
Unit 5 1B 143.93 m
500µm
C
Cal
Qtz
Qtz
Qtz
Units 4 & 5 1B 143.88 m
300µm
D
Qtz
Ttn
Pl
Cal
Cal
Cal
Cal
Unit 5 1B 143.92 m
200µm
E
Kfs
Kfs
Qtz
Pl
Kfs
Qtz
Qtz
Pl
Qtz
Pl
Unit 6d 1B 138.2 m
800µm
F
Zrn
Bt
Qtz
Ms
Ms
Bt
Bt
Ms
Qtz
Unit 6d 1B 142.24 m
300µm
G
Ttn
Qtz
Bt
Cal
Qtz
Ap
Qtz
Cal
Cal
Qtz
Bt + Msc
Unit 6d 1B 142.24 m
70µm
H
Cl
Qtz
Ttn
Bt
Qtz
Qtz
Ttn
Pl
Pl
Qtz
Cl
Pl
Bt
Qtz
Bt
Ttn
Pl
Qtz
Ep
Unit 7 DFDP1B 146.05 m
500µm

Figure 6.

Table 2. Qualitative X-Ray Diffraction Data for Selected Samples Recovered From DFDP-1A and DFDP-1B Core[a]

Hole Depth (m)	Lithology	Quartz	K Feldspar	Plagioclase	Muscovite	Biotite	Chlorite	Calcite	Ankerite	Spinel	Epidote
63.6	1	X		X	X		X	X			
66.7	2	X		X		X	X	X			
70.6	3	X		X	X		X				
74.5	4	X		X	X		X	X			
82.7	4	X		X	X		X	X			
86.35	4	X	X	X	X		X	X			
88.4	4	X		X	X		X	X			
89.34	4	X	X	X	X		X	X			
90.32	4	X	X	X	X		X	X			
90.62	5	X	X	X	X		X	X			
91.3	8	X		X	X	X	X				
112.12	3	X	X	X	X		X	X	X		
113.81	3	X		X	X		X				
116.72	3	X		X	X		X	X			
128.04	5	X			X		X	X		X	
128.09	5	X		X	X		X	X			
128.22	5	X		X	X		X	X			
128.5	6	X	X	X	X		X				
128.53	6	X	X	X	X		X				
128.80 w	6	X	X	X	X		X				
128.80 wg	6	X	X	X	X		X				
128.81	6	X	X	X	X		X				
130.88	6	X	X	X	X		X	X			
131.68	6	X	X	X	X		X				X
132.7	6	X	X	X	X		X				X
133.75	6	X	X	X	X		X				
140.96	6	X	X	X	X		X	X		X	
141.07	6	X	X	X	X		X				
141.77	6	X	X	X	X		X				X
141.9	6	X		X	X		X			X	
143.9	6	X		X	X		X	X			
144.02	7	X	X	X	X		X	X			
144.145	7	X	X	X	X		X				
144.28	7	X		X	X	X	X				

[a]Mineralogy of plagioclase and feldspar could not be discerned. No samples were available for the core interval below PSZ-2 in DFDP-1B, and those samples were analyzed with quantitative XRD (Table 3). For the two samples from 128.80 m, "w" and "gw" stand for white and green-white, the color of the specific sample.

calcite precipitated and 21.5 cm^3 per mol of goethite precipitated (Table 7). More detailed microstructural observations are needed to document the reaction sequences and their associated microstructures.

Although volume loss is commonly observed in fault cores, Alpine Fault rocks gained volume wherever calcite, illite, montmorillonite, and/or goethite precipitated (Figures 4 and 5 and Table 7) [e.g., *Goddard and Evans*, 1995; *Evans and Chester*, 1995; *Schleicher et al*., 2009; *Chen et al*., 2013; see also *Isaacs et al*., 2008]. On the Alpine Fault, solid volume gain from the precipitation of authigenic clay minerals and calcite from circulating hydrothermal fluids would act to decrease fault rock permeability with time (see section 5.5). Abundant evidence exists for the presence of vigorous hydrothermal system and advective fluid flow at depth east of the Alpine Fault beneath the Southern Alps [*Craw*, 1988; *Koons and Craw*, 1991; *Allis and Shi*, 1995; *Koons et al*., 1998; *Menzies et al*., 2016]. Multiple factors drive the Southern Alps hydrothermal system, including elevated isotherms, steep topography, abundant rainfall [*Barnes et al*., 1978; *Koons and Craw*,

Figure 6. Scanning electron microscope (SEM) backscattered electron (BSE) images of representative DFDP-1 fault rock lithologic units. Borehole depths are given on each image. 1A indicates DFDP-1A and 1B indicates DFDP-1B. (a) Unit 5 gouge containing reworked gouge clasts (gc). Several types of gouges occur within the central gouge clast. Other prominent clast types include variably altered Unit 2 ultramylonite, calcite, and potassium feldspar with inclusions of quartz and titanite. (b) Boudinaged and faulted hairline calcite-veins in a more competent Unit 5 gouge. (c) A boundary between a quartz-calcite clast in the Unit 6b lower foliated cataclasite and a Unit 5 gouge. Multiple fractures are sealed by calcite (arrows). (d) Gouge clast within a Unit 5 gouge. Calcite occurs as crenulated vein fragments and embayed clasts (arrows). Bright clast is coated in skeletal titanite. (e) Unit 6d lower cataclasite clasts derived from a granitoid protolith. Central clast is potassium feldspar with myrmekitic intergrowths of quartz in plagioclase. (f) Unit 6d lower cataclasite clast derived from a gneissic protolith. Note large ribbon quartz grains and muscovite, which is fracturing along cleavage planes and being incorporated into the matrix. (g) Unit 6d lower cataclasite matrix with rare calcite cement, which is more common near PSZ gouges. Overall, Unit 6 cataclasites are more porous than Unit 3 and 4 upper cataclasites (pores are black in BSE images). (h) Augen-bearing mylonite in the Unit 7 breccia. Foliation is defined by elongated quartz, chlorite, and plagioclase.

Table 3. Quantitative X-Ray Diffraction Data for Selected Samples Recovered From DFDP-1B Core[a]

Sample	Hole Depth (m)	Lithology	Quartz	K Feldspar	Plagioclase	Calcite	Kaolin	Smectite	White Mica	Chlorite	Amphibole	Pyrite	Total
36184	128	5 (PSZ1)	25	4	25	9	6	18	12		1	<1	99
36185	143.9	6/5 transition	41	<1	14	10			30	5		<1	100
36186	144.02	5 (PSZ2)	29	3	24	8		18	17	1		<1	100
36187	144.14	5 (PSZ2)	36	4	23	5		15	15	2		<1	100
36188	144.15	5/7 transition	33	2	36				26	3		<1	100
36189	144.28	7	34	2	35	2				4		<1	77

[a]Mineralogy of plagioclase and feldspar could not be discerned. The dioctahedral smectite present is montmorillonite-15Å. Chlorite is clinochlore-1MIIB, and the amphibole is actinolite. Amorphous phases were not identified and results are normalized to 100%. All samples from the DFDP-1B borehole, latitude/longitude coordinates 43.3141°S/170.3259°E.

1991; *Menzies et al*., 2014, 2016], production of overpressured metamorphic fluids at depth [*Craw and Campbell*, 2004; *Vry et al*., 2001, 2009], and perhaps coseismic increases in fault rock permeability accompanied by overpressured metamorphic fluid migration [*Sibson*, 1992; *Townend et al*., 2013]. Within this system, rising rock-exchanged and mantle-derived fluids mix with descending meteoric waters and emerge in the fault's hanging wall as warm springs [*Barnes et al*., 1978; *Templeton et al*., 1998; *Upton et al*., 1995; *Menzies et al*., 2014, 2016] (Figure 11).

5.2. Major Element Geochemistry Variations

Major element geochemistry results presented in Figures 7–9 have not been normalized to account for changes in relative element abundance based on silica mobility in the fault zone [e.g., *Gresens*, 1967; *Grant*, 1986]. TiO_2 is commonly assumed to be immobile in fault zones [e.g., *Schleicher et al*., 2009], but normalizing major element oxides to TiO_2 requires assuming a value for a single unaltered protolith. Moreover, neometamorphic titanite that postdates chloritization of Alpine Fault mylonites at high temperatures (~425–500°C) has been identified [*Vry et al*., 2001]. Nevertheless, the major element data reveal trends within the DFDP-1 lithologic units. The Unit 5 gouges have lower SiO_2, higher CaO concentrations, and anomalously high LOI values when compared to adjacent hanging wall and footwall lithologic units (Figures 7 and 8). These measurements corroborate our petrographic and XRD identification of retrograde clay minerals (illite and montmorillonite) and calcite cement in the PSZ gouges (Table 3, Figures 6a, 6b, and 6d).

The DFDP-1A Unit 5 gouge at 90.62 m and the DFDP-1B Unit 6 lower cataclasites have higher K_2O contents than background hanging wall material (Figures 7 and 8). The Unit 6 lower cataclasites were derived in part from granitoid protoliths rich in quartz, plagioclase, and K-feldspar, and thus reflect the chemistry of these minerals (the Australian Plate Karamea Suite) (cf., Figures 4e, 5e, and 9). The presence of elevated K_2O in the DFDP-1A PSZ gouges provides evidence for incorporation of footwall K-feldspar, adularia, and/or potassic pseudotachylyte, which is common within cataclasites at Gaunt Creek [*Norris and Cooper*, 2007; *Toy et al*., 2011]. In addition, the major element geochemistry K_2O data are supported by XRD and/or thin section observations of K-feldspar in this unit and in the Unit 4 upper foliated gouges up to 5 m from the PSZ (Table 2, Figures 4b, 5a, and 5b).

Further trace element and isotopic investigations are required to determine the origin of the Unit 7 breccia. Despite being the lowest structural unit in the boreholes, the Unit 7 breccia shares the same mineral assemblage as both the upper (Unit 3 and Unit 4) and lower (Unit 6) catalcasites (quartz + potassium feldspar + plagioclase + biotite + chlorite + muscovite ± epidote + accessory minerals) (Tables 1 and 2). In thin section, Unit 7 contains visibly more graphite and apatite than the other lithologic units, the latter being reflected in elevated P_2O_5 concentrations (Table 6, Figures 4h, and 8). However, the two Unit 7 samples lie at the intersection of the hanging wall and footwall trends in Figure 9.

The major element geochemistry of fault rocks retrieved from the DFDP drillholes and collected from nearby natural exposures generally reflects the composition of the metamorphic or plutonic protoliths [*Roser and Cooper*, 1990; *Roser and Korsch*, 1999; *McClintock and Cooper*, 2003; *Pitcairn et al*., 2006] (Figure 9). Because fault rocks within the fault core and damage zone are derived from multiple protoliths and have experienced multiple phases of deformation, including exhumation and dextral translation along the Alpine Fault [*Little et al*., 2005; *Cooper and Norris*, 2011], it is difficult to ascertain the original composition of the fault rocks, the nature of fluid mobility through time, and the amount of mass gained and lost [e.g., *O'Hara*,

AGU Geochemistry, Geophysics, Geosystems

10.1002/2016GC006588

Table 4. Quantitative X-Ray Diffraction Data for Cataclasites and Fault Gouges Collected at Localities Along Strike of the Central and Southern Alpine Fault[a]

Sample	Location	Lithology	Fraction	Quartz	K Feldspar	Plagioclase	Calcite	Mg-Calcite	Ankerite	Kaolin	Smectite	White Mica	Chlorite	Serpentine	Talc	Amphibole	Pyrite	Laumontite	Total
36959	Little Man R.	5	WR	18	3	33	10			6	20	10							100
34103	Gaunt Ck Terrace	5	WR	35	<1	17	6					32	9						99
34103_2	Gaunt Ck Terrace	5	< 2 μm	5		3						50	42						100
35067	Gaunt Ck Scarp	3	WR	49	10	19	2		12	8				<1					100
34113	Gaunt Ck Scarp	3	< 2 μm	<1								68	32						100
34112	Gaunt Ck Scarp	4fol	< 2 μm	9	3	27	2			4	36	16	2						99
34104	Gaunt Ck Scarp	5	WR	30	6	26	7	1		6	7	17							100
34119	Gaunt Ck Scarp	5	< 2 μm	8		16					29	17	29						99
34105	Gaunt Ck Scarp	5ucl	WR	25	5	20	5			7	14	16		8					100
34117	Stoney Ck	3	< 2 μm	4	<1	7	8					41	40						100
35363	Waikukupa R	4	WR	35	33	6			1			6	19				<1	<1	100
34114	Waikukupa R	4	< 2 μm	4		19	2					21	51					2	99
34106	Waikukupa R	5	WR	28		26	25		<1			14	5			2	<1		100
34118	Waikukupa R	5	< 2 μm	8	<1	10	10				24	26	22						100
34107	Waikukupa R	5ucl	WR	27	1	19	17				16	17	2				<1		99
34108	Waikukupa R	5	WR	27	<1	20	16				13	20	4				<1		100
36962	Robinson Ck	4	WR	40	14	21	4					17	5						101
36961	Robinson Ck	5	WR	32	6	32					19	7	2			3			101
36960	Robinson Ck	8	WR	35	2	41						16	2			5			101
34109	Martyr R	5fol	WR	8	4	15	<1					35	39				<1		101
34958	Martyr R	5	WR	37	4	7	1					36	15						100
34115	Martyr R	5	< 2 μm	2								70	28						100
34111	McKenzie Ck	5	WR	8	1	1	5				61[b]		11	13					100
34110	Hokuri Ck	4rim	WR	<1			2						5	93					100
34959	Hokuri Ck	5	WR	2			5				74[b]		3	12	2	2			26
34116	Hokuri Ck	5	< 2 μm								78[b]			21	1				22

[a]Sample 34119 was from a weathered block and was not a separate from sample 34104. Lithologic units are described in the text. Abbreviations are: fol, foliations present; ucl, the most highly comminuted, striated gouge that marks the HW/FW contact; rim, a foliated cataclasite present on the rim of a serpentinite pod. WR denotes whole rock, and < 2 μm denotes clay-sized fraction. Mineralogy of plagioclase and feldspar could not be discerned. The dioctahedral smectite present is montmorillonite-15Å. Chlorite is clinochlore-1MIIB, the serpentine is lizardite-1M, and the amphibole is actinolite. There was insufficient kaolin present to discern kaolinite from dickite. Amorphous phases were not identified, and results are normalized to 100%. Location latitude/longitude coordinates are: Little Man River 43.1400°S/170.2818°E; Gaunt Creek Terrace and Gaunt Creek Scarp 43.3141°S/170.3259°E; Stoney Creek 43.2290°S/170.1239°E; Waikukupa River 43.2622°S/170.0490°E; Robinson Creek 43.4956°S/169.1350°E; Martyr River 44.1326°S/168.5536°E; McKenzie Creek 44.3599°S/168.1390°E; Hokuri Creek 44.4062°S/168.0648°E.

[b]Smectite mineral present is trioctahedral saponite.

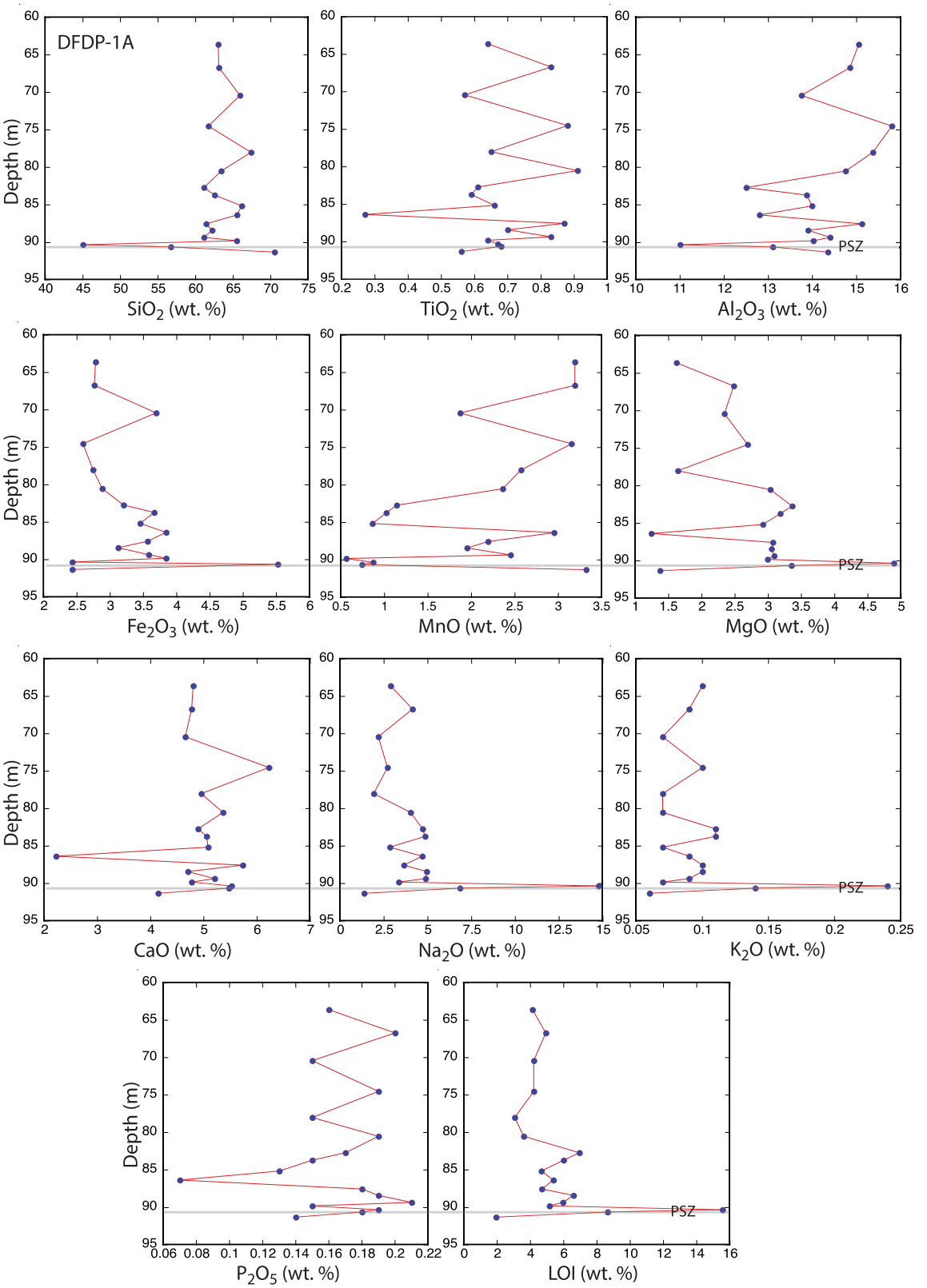

Figure 7. Variations in relative major element oxide abundance, given as wt. %, with depth in DFDP-1A. A semitransparent gray line marks the depth of the Unit 5 PSZ gouge (labeled PSZ), which is the contact between hanging wall lithologic units (Units 1–5) and footwall gravels (Unit 8). See text for details.

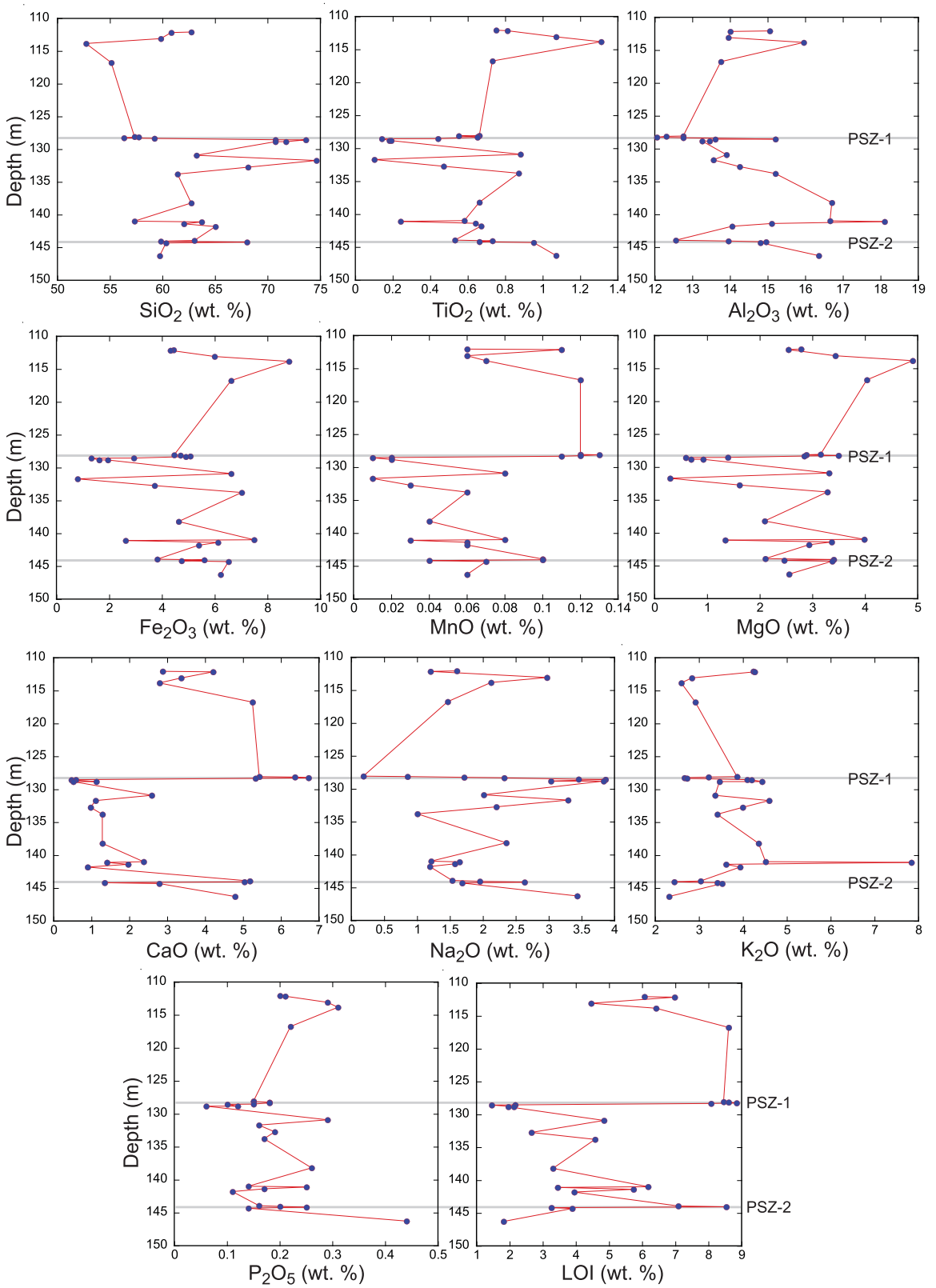

Figure 8. Variations in relative major element oxide abundance, given as wt. %, with depth in DFDP-1B. A semitransparent gray line marks the depth of the Unit 5 PSZ-1 gouge (labeled PSZ-1), which is the contact between hanging wall lithologic units (Units 1–5) and footwall lithologic units (Units 6 and 7). Another semitransparent gray line marks the depth of the Unit 5 PSZ-2 gouge (labeled PSZ-2), which is the contact between Unit 6 footwall cataclasites and Unit 7 footwall breccia. See text for details.

Table 5. Major Element Geochemistry of DFDP-1A Samples From XRF and ICP-AES Analysis[a]

Sample	Hole Depth (m)	Lithology	SiO_2	TiO_2	Al_2O_3	Fe_2O_3t	MnO	MgO	CaO	Na_2O	K_2O	P_2O_5	Cr_2O_3	SrO	BaO	LOI	Total
DFDP1	63.6	1	63.0	0.64	15.05	4.80	0.10	1.62	2.87	3.19	2.78	0.16	0.01	0	0.1	4.12	98.46
DFDP2	66.7	2	63.1	0.83	14.85	4.77	0.09	2.48	4.12	3.19	2.76	0.20	0.01	0.1	0.1	4.92	101.46
DFDP3	70.4	3	65.9	0.57	13.75	4.65	0.07	2.34	2.17	1.87	3.69	0.15	0.01	0	0.1	4.20	99.46
DFDP4	74.5	4	61.7	0.88	15.80	6.22	0.10	2.69	2.69	3.15	2.59	0.19	0.01	0	0.1	4.20	100.34
RW_XRF	78	2	67.4	0.65	15.37	4.95	0.07	1.64	1.91	2.57	2.74	0.15	NA	NA	NA	3.05	100.48
RW_XRF	80.5	4	63.4	0.91	14.75	5.36	0.07	3.03	4.01	2.36	2.88	0.19	NA	NA	NA	3.59	100.55
DFDP5	82.7	4	61.1	0.61	12.50	4.89	0.11	3.36	4.7	1.14	3.2	0.17	0.01	0	0	6.94	98.80
RW_XRF	83.7	4	62.5	0.59	13.87	5.05	0.11	3.18	4.84	1.02	3.66	0.15	NA	NA	NA	5.99	100.99
RW_XRF	85.15	4	66.1	0.66	13.99	5.08	0.07	2.92	2.83	0.86	3.45	0.13	NA	NA	NA	4.65	100.78
DFDP6	86.35	4	65.5	0.27	12.80	2.22	0.09	1.24	4.68	2.95	3.84	0.07	0.01	0	0.1	5.38	99.13
RW_XRF	87.54	4	61.4	0.87	15.12	5.73	0.10	3.07	3.63	2.19	3.56	0.18	NA	NA	NA	4.68	100.52
DFDP7	88.4	4	62.2	0.7	13.90	4.70	0.10	3.05	4.93	1.95	3.12	0.19	0.01	0	0	6.59	101.51
DFDP8	89.34	4	61.1	0.83	14.40	5.20	0.09	3.09	4.87	2.45	3.58	0.21	0.01	0.1	0.1	5.95	101.94
RW_XRF	89.8	4	65.5	0.64	14.02	4.77	0.07	2.99	3.34	0.56	3.84	0.15	NA	NA	NA	5.14	100.99
DFDP9	90.32	4	45.0	0.67	11.00	5.52	0.24	4.89	14.8	0.87	2.43	0.19	0.01	0.1	0	15.55	101.21
DFDP10	90.62	5	56.7	0.68	13.10	5.47	0.14	3.35	6.83	0.74	5.52	0.18	0.01	0	0.1	8.64	101.53
DFDP11	91.3	8	70.5	0.56	14.35	4.14	0.06	1.37	1.36	3.32	2.43	0.14	0.01	0	0.1	1.93	100.26

[a]All values are in wt. %. Fe_2O_3t denotes total Fe_2O_3. NA denotes not analyzed. All "DFDP" samples analyzed with ICP-AES; instrument precision for this method is ±0.02 wt.%. Analytical error for this method varies with major element oxide and sample abundance of major element oxide. Repeat standard analyses yield the following maximum analytical errors: SiO_2 ±2.20%; TiO_2 ±1.55%; Al_2O_3 ±2.68%; Fe_2O_3 ±2.52%; MnO ±0.01%; MgO ±1.60%; CaO ±5.44%; Na_2O ±9.00%; K_2O ± 2.53%. Other oxide abundances (wt. %) were within instrument precision with analytical errors up to 100%. "RW_XRF" samples were analyzed with XRF; instrument precision for this method was not available. Repeat standard analyses yield the following maximum analytical errors: SiO_2 ±0.20%; TiO_2 ±0.44%; Al_2O_3 ±0.34%; Fe_2O_3 ±0.21%; MnO ±10.88%; MgO ±2.32%; CaO ±0.44%; Na_2O ±8.32%; K_2O ± 0.60%. A maximum LOI analytical error ±11.55% was calculated from repeat standard analyses provided by ALS Minerals. LOI, listed as percentage by weight, is a measure of the volatile content of the samples, and this measurement includes the weight loss due to both dehydration and decarbonation reactions.

Table 6. Major Element Geochemistry of DFDP-1B Samples From ICP-AES Analysis[a]

Sample	Hole Depth (m)	Lithology	SiO_2	TiO_2	Al_2O_3	Fe_2O_3t	MnO	MgO	CaO	Na_2O	K_2O	P_2O5	Cr_2O_3	SrO	BaO	LOI	Total
DFDP12	112.04	4	62.7	0.75	15.05	4.43	0.06	2.78	2.87	1.6	4.23	0.2	0.01	0.03	0.06	6.06	100.8
DFDP13	112.12	3	60.8	0.81	14.00	4.31	0.11	2.54	4.2	1.2	4.26	0.21	0.01	0.03	0.05	6.97	99.5
DFDP14	113.05	3	59.8	1.07	13.95	5.98	0.06	3.43	3.36	2.97	2.83	0.29	0.02	0.05	0.09	4.45	98.35
DFDP15	113.81	3	52.7	1.31	15.95	8.80	0.07	4.9	2.79	2.12	2.59	0.31	0.03	0.03	0.04	6.41	98.05
DFDP16	116.72	3	55.1	0.73	13.75	6.61	0.12	4.03	5.24	1.46	2.91	0.22	0.01	0.04	0.04	8.6	98.86
DFDP17	128.04	4	57.3	0.66	12.75	4.45	0.12	3.15	5.42	0.18	3.86	0.15	0.02	0.02	0.03	8.45	96.56
DFDP18	128.09	4	57.7	0.55	12.30	4.69	0.13	2.88	6.36	0.85	3.21	0.15	0.01	0.02	0.02	8.6	97.47
DFDP19	128.22	4	56.3	0.65	12.05	5.06	0.12	3.49	6.72	1.71	2.66	0.18	0.01	0.04	0.04	8.84	97.87
DFDP20	128.3	5	59.2	0.65	12.75	4.89	0.11	2.84	5.32	2.32	2.72	0.18	0.01	0.06	0.07	8.07	99.19
DFDP21	128.5	6	70.7	0.44	15.20	2.92	0.02	1.39	0.58	3.45	4.09	0.15	0.01	0.04	0.08	2.16	101.2
DFDP22	128.53	6	73.6	0.14	13.60	1.31	0.01	0.59	0.46	3.86	4.19	0.1	<0.01	0.03	0.08	1.45	99.42
DFDP23	128.8	6	71.7	0.18	13.45	1.61	0.02	0.69	1.12	3.03	4.43	0.12	<0.01	0.03	0.07	2.12	98.57
DFDP24	128.8	6	70.7	0.19	13.25	1.94	0.02	0.92	0.51	3.83	3.46	0.06	0.01	0.03	0.07	1.95	96.94
DFDP25	130.88	6	63.2	0.88	13.90	6.61	0.08	3.31	2.58	2.01	3.36	0.29	0.03	0.03	0.07	4.84	101.2
DFDP26	131.68	6	74.6	0.1	13.55	0.79	0.01	0.29	1.1	3.29	4.59	0.16	<0.01	0.03	0.07	NSS	NSS
DFDP27	132.7	6	68.1	0.47	14.25	3.71	0.03	1.61	0.97	2.2	3.99	0.19	0.01	0.03	0.07	2.65	98.28
DFDP28	133.75	6	61.4	0.87	15.20	7.01	0.06	3.28	1.28	1.00	3.41	0.17	0.02	0.02	0.06	4.57	98.35
DFDP29	138.17	6	62.7	0.66	16.70	4.62	0.04	2.09	1.28	2.35	4.35	0.26	0.01	0.02	0.06	3.3	98.44
DFDP30	140.96	6	57.3	0.58	16.65	7.48	0.08	3.98	2.37	1.21	4.51	0.14	0.03	0.02	0.06	6.17	100.6
DFDP31	141.07	6	63.7	0.24	18.10	2.61	0.03	1.34	1.40	1.64	7.83	0.25	<0.01	0.02	0.1	3.44	100.7
DFDP32	141.35	6	62.0	0.64	15.10	6.11	0.06	3.36	1.96	1.57	3.61	0.17	0.02	0.02	0.07	5.73	100.4
DFDP33	141.77	6	65.0	0.67	14.05	5.38	0.06	2.93	0.89	1.19	3.93	0.11	0.02	0.02	0.1	3.94	98.29
DFDP34	141.9	6	NSS	NSS	NSS	NSS	NSS	NSS	NSS	NSS	NSS	NSS	NSS	NSS	NSS	4.73	NSS
DFDP35	143.9	6	63.0	0.53	12.55	3.81	0.1	2.10	5.17	1.53	3.03	0.16	0.01	0.02	0.03	7.08	99.12
DFDP36	144.02	5	59.8	0.73	13.95	5.59	0.1	3.40	5.03	1.95	2.43	0.2	0.02	0.08	0.09	8.53	101.9
DFDP37	144.15	5	68.0	0.66	14.95	4.73	0.04	2.46	1.34	2.63	3.41	0.25	0.01	0.04	0.07	3.25	101.8
DFDP38	144.28	7	60.3	0.95	14.80	6.51	0.07	3.37	2.78	1.68	3.52	0.14	0.02	0.03	0.14	3.88	98.19
DFDP39	146.25	7	59.7	1.07	16.35	6.21	0.06	2.55	4.78	3.43	2.31	0.44	0.03	0.09	0.11	1.81	98.94

[a]All values are in wt. %. Fe_2O_3t denotes total Fe_2O_3. NSS denotes not sufficient sample. Instrument precision and analytical error as reported in the Table 5 caption.

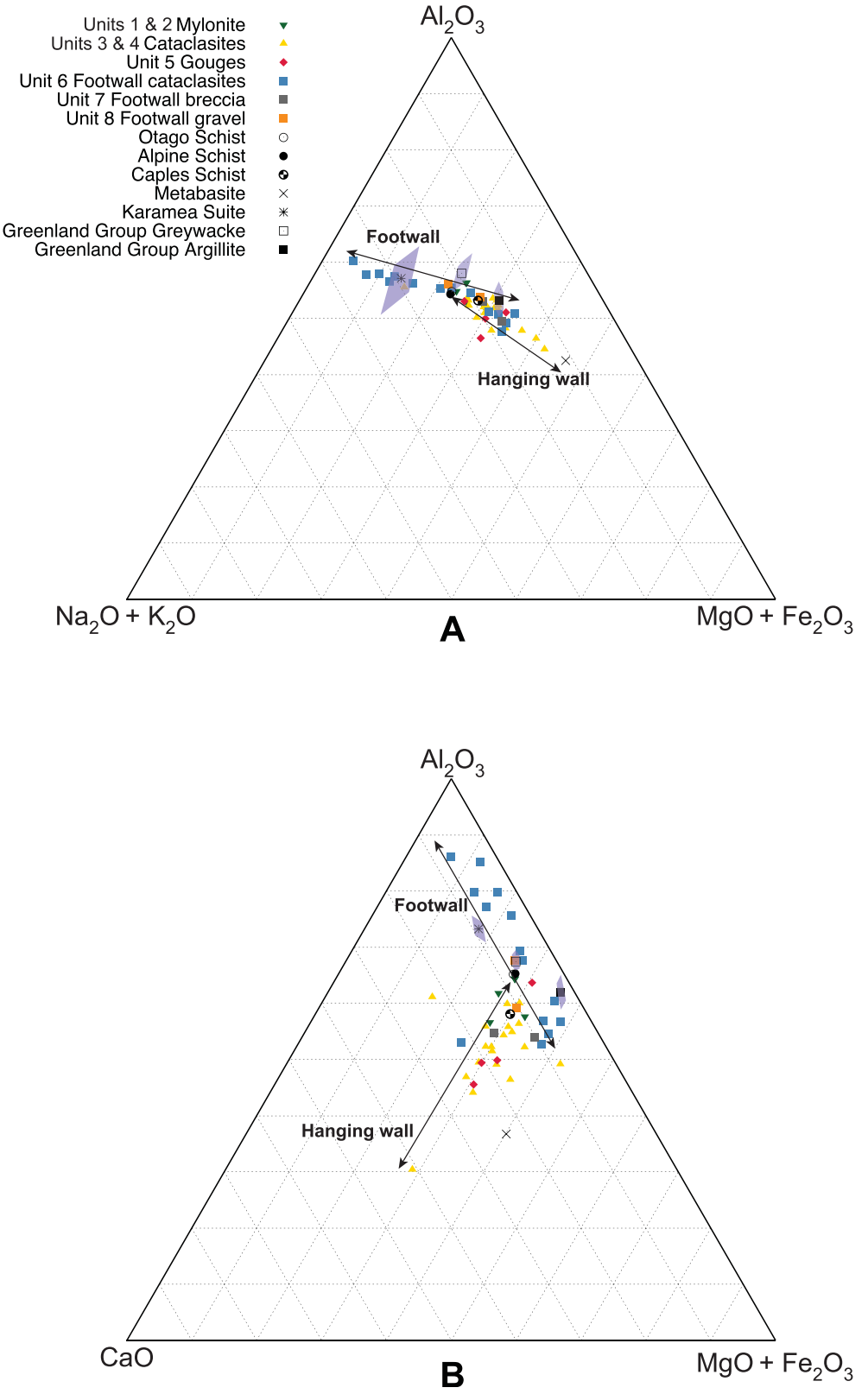
Units 1 & 2 Mylonite
Units 3 & 4 Cataclasites
Unit 5 Gouges
Unit 6 Footwall cataclasites
Unit 7 Footwall breccia
Unit 8 Footwall gravel
Otago Schist
Alpine Schist
Caples Schist
Metabasite
Karamea Suite
Greenland Group Greywacke
Greenland Group Argillite
Al2O3
Footwall
Hanging wall
Na2O + K2O
MgO + Fe2O3
A
Al2O3
Footwall
Hanging wall
CaO
MgO + Fe2O3
B

Figure 9.

1988; *Ague*, 1994; *Evans and Chester*, 1995] (Tables 5 and 6, Figure 9). In order to asses original rock protolith compositions and constrain geochemical variability due to fluid-rock interactions—thus resulting in estimates for mass loss and mass gain in the fault zone—further research involving immobile trace elements and radiogenic isotopes is required.

5.3. Effect of Alteration Reactions on Fault Zone Rheology

Marking the transition from the damage zone to alteration zone, Unit 1 and 2 ultramylonites exhibit microstructures indicative of deformation by dislocation creep; a retrogressed mineral assemblage in Unit 2 indicates some alteration took place in this lithologic unit [e.g., *Prior*, 1988; *Norris and Cooper*, 2007; *Toy et al*., 2008, 2015] (Figure 3). Within the alteration zone, brittle deformation involving cataclasis has formed Unit 3 upper unfoliated cataclasites, some of which show evidence of sealing via multiple generations of carbonates, which are comparatively sparse in the Alpine Fault mylonite sequence (A. Cooper, personal communication, 2012) (Figures 5c, 7, and 8). Shear deformation of comminuted and precipitated phyllosilicate minerals, particularly chlorite and white mica, has also resulted in the formation of networks of anastomosing phyllosilicates (Unit 4 upper foliated cataclasites) (Figures 4c 4d, and 5g). However, in the Unit 5 fault gouges, these foliations have been disrupted by cataclasis. Furthermore, chlorite and potassium feldspar have altered to montmorillonite in these gouges; potassium feldspar and/or albite have also reacted to form kaolinite (Tables 3 and 4) (e.g., Figures 6a–6d).

Alpine Fault mineralogical and structural variations have rheological implications best understood in the context of similar natural and analog fault rocks. Fault cores containing gouges (or ultracataclasite) bounded by foliated cataclasites have been described from many inactive fault zones, including the Geesaman fault zone, Arizona, USA, exhumed from $<$13 km depth [*Janecke and Evans*, 1988; *Schulz and Evans*, 1998, 2000], the Punchbowl Fault, California, USA, exhumed from 2 to 4 km depth [*Chester et al*., 1993], the Median Tectonic Line, Japan, exhumed from 5 to 10 km depth [*Jefferies et al*., 2006], and the Zuccale Fault, exhumed from $<$8 km depth [*Collettini and Holdsworth*, 2004]. Within these fault cores, the brecciation and/or cataclasis of fault zone protolith(s) created fluid migration pathways, triggering phyllosilicate mineralization via fluid-assisted hydration reactions [e.g., *Janecke and Evans*, 1988]. When phyllosilicate minerals form an interconnected fabric with a preferred orientation of (001) parallel to the shearing direction, frictional sliding can occur at low resolved shear stresses because of weak (001) interlayer bond strengths and/or adsorbed water films [e.g., *Moore and Lockner*, 2004; *Collettini et al*., 2009; *Tembe et al*., 2010].

At higher temperatures and pressures, at depths of 3 to 15 km that encompass the brittle-to-plastic transition, strain-rate and grain-size-dependent diffusion-assisted pressure solution creep (also termed "grain size sensitive creep") may operate in foliated fault rocks [e.g., *Sibson*, 1977; *Chester and Higgs*, 1992; *Hickman et al*., 1995; *Bos and Spiers*, 2002]. Microphysical models of this mechanism predict the shear strength of foliated fault rocks, such as the Unit 4 foliated cataclasites, is governed by: resistance to shear along phyllosilicate foliations; solution transfer in rigid mineral grains; or dilation as sliding foliate are forced to overcome geometrical incompatibilities [*Bos and Spiers*, 2002]. Analog experiments conducted to high-strain have shown that the development of a through-going phyllosilicate foliation coupled with diffusive pressure solution creep can reduce fault zone strength by 50–70% below Byerlee values ($\mu \approx 0.85$) [*Bos and Spiers*, 2002; *Niemeijer and Spiers*, 2005]. However, this mechanism will only operate in foliated gouges and/or

Figure 9. Ternary plots of variations in major element geochemistry for samples analyzed from DFDP-1A and DFDP-1B. All units are wt. %. Hanging wall fault-related rocks are grouped: Units 1 and 2 mylonites (green down triangles), and Units 3 and 4 cataclasites (yellow up triangles). Unit 5 gouges (DFDP-1A PSZ, DFDP-1B PSZ-1, and PSZ-2) are grouped together (red diamonds). Footwall lithologic units are: Unit 6 footwall cataclasites (green squares), Unit 7 footwall breccia (grey squares), and Unit 8 footwall gravels (orange squares). Also plotted are average hanging wall protolith, Otago Schist (n = 38), Alpine Schist (n = 25), Caples Schist (n = 20), and metabasite (n = 18) compositions from *Pitcairn* [2004]. Average footwall protolith, Karamea Suite granitoids, Greenland Group greywacke and argillite, compositions were calculated from data in PETLAB, most of which were published in *Nathan* [1976], *Roser et al*. [1995], *Tulloch and Palmer* [1990], and *Tulloch et al*. [2009] (results downloaded from PETLAB http://pet.gns.cri.nz). Purple-shaded regions around each footwall protolith composition represent $\pm 1\sigma$. (a) A ternary plot of Al_2O_3-Na_2O+K_2O-MgO+Fe_2O_3 variations. Hanging wall lithologic units follow a trend between Otago Schist/Alpine Schist and metabasite protolith compositions; the hanging wall cataclasites are relatively more enriched in MgO+Fe_2O_3. Footwall lithologic units follow a trend between Unit 7 footwall breccia and Karamea Suite protolith, but some Unit 6 cataclasites are relatively enriched in Al_2O_3-Na_2O+K_2O. (b) A ternary plot of Al_2O_3-CaO-MgO+Fe_2O_3 variations. Hanging wall lithlogic units do not follow a trend between protolith compositions, but rather follow a trend from Otago Schist/Alpine Schist protolith composition towards relative CaO-enrichment. A single footwall catclasite, from DFDP-1B 143.9 m immediate above PSZ-2, has a higher amount of CaO. Footwall lithologic units follow a trend between Unit 7 footwall breccia/Greenland Group argillite and Karamea Suite protolith, but some Unit 6 cataclasites have relatively more Al_2O_3.

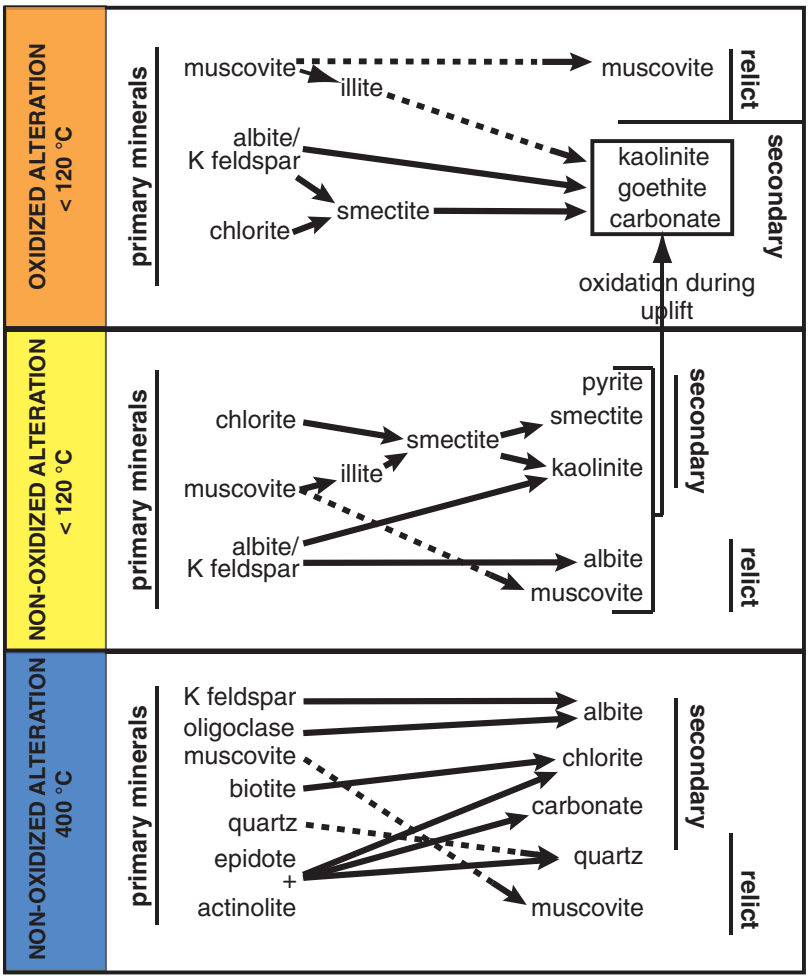

Figure 10. During exhumation from subgreenschist facies temperatures and pressures, Alpine Fault cataclasites and gouges have undergone multiple phases of alteration. Following *Warr and Cox* [2001] and *Chamberlain et al*. [1999], primary nonoxidized and oxidized alteration reactions are outlined in the figure. K-feldspar is not present in Alpine or Otago Schist protoliths, but it is observed in DFDP-1A and DFDP-1B lithologic units, particularly below PSZ-2 in DFDP-1B. See text for more details.

Table 7. Balanced Alteration Reactions and Solid Volume Changes Associated With Each Reaction[a]

Reaction	ΔV_{solid} (cm^3)	ΔV_{solid} (%)
1. K-feldspar + Na^+ = Albite + K^+	−9	−8
2. 3albite + $2H^+$ + K^+ = muscovite + $6SiO_2$ + $3Na^+$	−23	−8
3. 3K-feldspar + $2H^+$ = muscovite + $6SiO_2$ + $2K^+$	−49	−15
4. 2phlogopite + $4H^+$ + H_2O = clinochlore + $2SiO_2$ + Mg^{2+} + $2K^+$	−25	−8
5. phlogopite + $6H^+$ = K-feldspar + $3Mg^{2+}$ + $4H_2O$	−41	−27
6. 2K-feldspar + $5Mg^{2+}$ + $8H_2O$ = clinochlore + $3SiO_2$ + $2K^+$ + $8H^+$	61	30
7. 3clinochlore + $2K^+$ + $28H^+$ = 2muscovite + $3SiO_2$ + $15Mg^{2+}$ + $24H_2O$	−272	−44
8. 3muscovite + 5biotite + $9SiO_2$ + $4H_2O$ = 8K-feldspar + 3clinochlore	−41	−2.7
9. 2K-feldspar + $6H^+$ = kaolinite + $2K^+$ + $4SiO_2$ + $3H_2O$	−30	−13.7
10. 2albite + $6H^+$ = kaolinite + $2Na^+$ + $4SiO_2$ + $3H_2O$	−12.5	−6.2
11. 5.5muscovite + H^+ = 3illite + K^+ + $3SiO_2$	12.5	6.9
12. clinochlore + 3K-feldspar + H_2O + $9H^+$ = 3montmorillonite + $3Mg^{2+}$ + $3K^+$	41.8	8.1

[a]All reactions balanced assuming simplified end-member mineral formula. Calculated solid volume changes assume the product SiO_2 precipitates as quartz; however, SiO_2 can leave the reaction site as an aqueous species. Iron may be present in clinochlore and montmorillonite minerals, but reactions are balanced assuming only octahedral magnesium cations. Reactions 1–8 from *Wintsch and Yeh* [2013]. End-member formulas from *Holland and Powell* [1998]; end-member illite formula from *Deer et al.* [1992]. Note the density of phyllosilicate minerals can vary with cation ratio and interlayer hydration state [e.g., *Totten et al*., 2002].

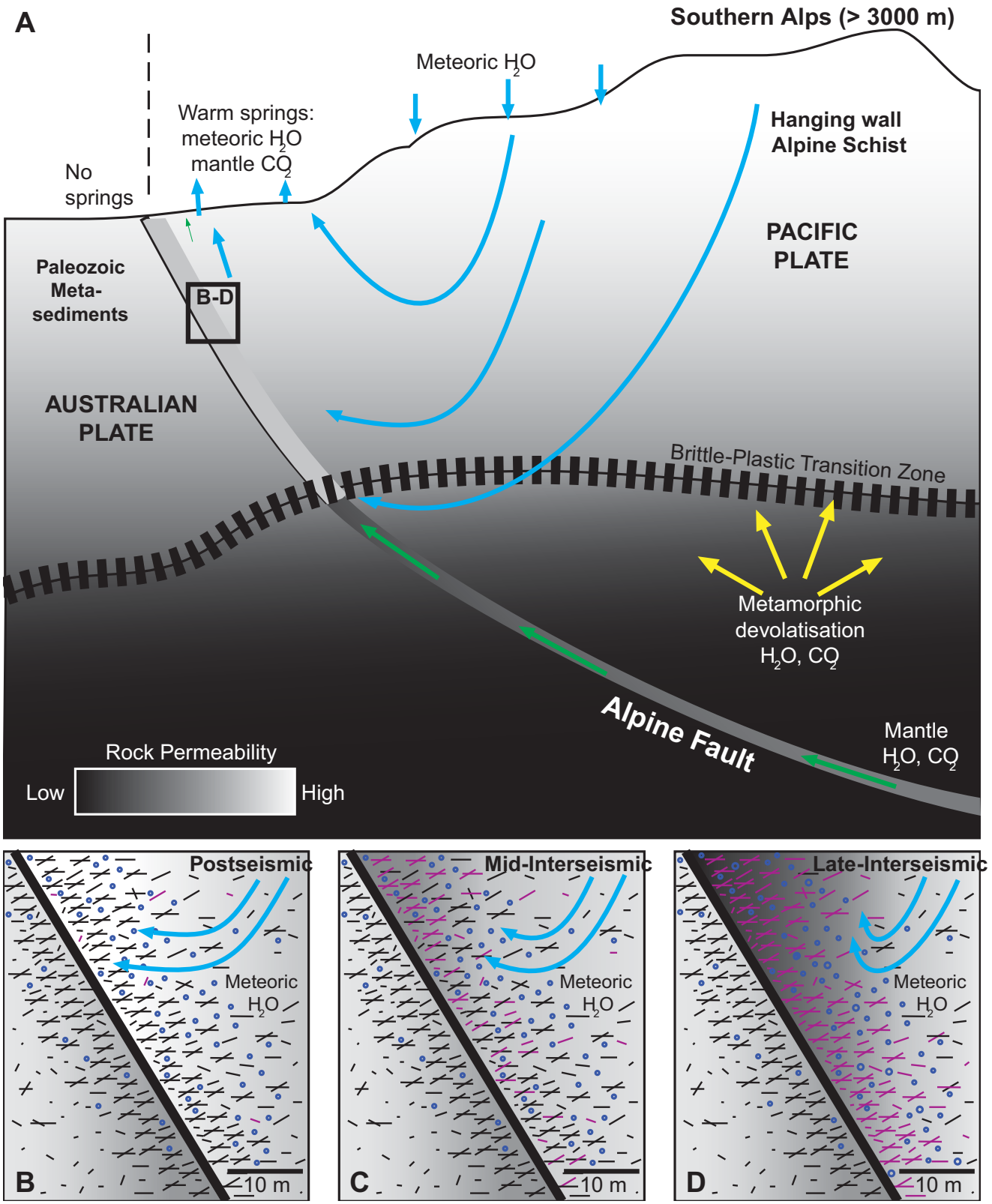
A
Southern Alps (> 3000 m)
Meteoric H2O
Warm springs:
meteoric H2O
mantle CO2
No
springs
Hanging wall
Alpine Schist
PACIFIC
PLATE
Paleozoic
Meta-
sediments
B-D
AUSTRALIAN
PLATE
Brittle-Plastic Transition Zone
Metamorphic
devolatisation
H2O, CO2
Alpine Fault
Mantle
H2O, CO2
Rock Permeability
Low
High
Postseismic
Meteoric
H2O
B
10 m
Mid-Interseismic
Meteoric
H2O
C
10 m
Late-Interseismic
Meteoric
H2O
D
10 m

Figure 11.

cataclasites at low sliding velocity when the phyllosilicate foliation is interconnected and the rate of mass removal by pressure solution is fast enough to accommodate shear. Phyllosilicate foliations are disrupted at experimental sliding velocities >0.3–1 μm/s (equivalent strain rates >0.3–1 s^{-1}) [*Bos and Spiers*, 2001; *Niemeijer and Spiers*, 2005].

The frequent juxtaposition of Unit 3 nonfoliated cataclasites and Unit 4 foliated cataclasites within DFDP-1 drillcore may reflect deformation accommodated at various sliding velocities within these materials (Figures 3 and 4a). However, the occurrence of recycled fault gouge clasts, relict pseudotachylyte, and enhanced alteration in the smectite-bearing Unit 5 PSZ gouges suggest that repeated slip events occurred preferentially in these materials (e.g., Figures 4g and 6a). Therefore, understanding the frictional properties of the Unit 5 gouges remains a primary research objective [*Boulton et al*., 2012, 2014; *Niemeijer et al*., 2016]. Although there is currently no evidence that aseismic creep occurs on the Alpine Fault, observations are limited to the past 50 years, a time span covering the late interseismic phase of the seismic cycle [*Evison*, 1971; *Sutherland et al*., 2007; *Beavan et al*., 1999, 2010; *Lamb and Smith*, 2013]. It is possible that temporal variations in pore fluid pressure, effective normal stress, shear stress, sliding velocity, and pore fluid chemistry promote the operation of mechanically diverse deformation mechanisms [e.g., *Smith et al*., 2011; *Rowe et al*., 2011].

5.4. Effect of Alteration Reactions on Fault Zone Permeability

Fault-normal permeability of hanging wall materials decreases with proximity to the highly impermeable Unit 5 PSZ gouges (from $\sim 10^{-15}$ m^2 to 10^{-20} m^2) [*Carpenter et al*., 2014]. These permeability data correspond with the decrease in grain size, an increase in abundance of fault parallel (or subparallel) fine-grained foliations, and/or an increase in pore-infilling, fracture-sealing clay minerals and carbonate with proximity to the PSZ gouges (Figures 4–6) [*Sutherland et al*., 2012; *Townend et al*., 2013; *Carpenter et al*., 2014]. Within alteration zone-fault core lithologic units (Units 2–6), solution-assisted compaction might also lead to significant porosity reduction, further decreasing permeability and promoting pore fluid pressurization, which is another viable weakening mechanism [e.g., *Sibson*, 1991; *Sleep and Blanpied*, 1992; *Wibberley and Shimamoto*, 2003] (e.g., Figures 4c and 4d). A time-dependent increase in pore fluid pressure within frictionally strong fault material is compatible with repeating seismic failure without the operation of intervening aseismic creep, a deformation pattern consistent with current paleoseismological records of Alpine Fault seismicity [e.g., *Sutherland et al*., 2007; *Berryman et al*., 2012; *Howarth et al*., 2012].

5.5. Implications for the Alpine Fault Seismic Cycle

Temporal variations in pore fluid pressure can be visualized in the context of an earthquake cycle-model (Figure 11). The creation of fractures within hanging wall and footwall fault-related rocks during an earthquake increases permeability and promotes fluid migration within the alteration zone [e.g., *Caine et al*., 1996; *Chester and Chester*, 1998; *Mizoguchi and Ueta*, 2013]. While permeability is likely to increase within alteration and damage zone lithologic units during a seismic event, high velocity sliding can either decrease PSZ gouge permeability through shear-induced compaction [*Tanikawa et al*., 2012] or increase PSZ gouge permeability through shear or thermal pressurization-induced dilation [e.g., *Segall and Rice*, 1995; *Samuelson et al*., 2009; *Garagash*, 2012; *Platt et al*., 2015]. Within the alteration zone, migration of carbonate-saturated meteoric fluids in chemical disequilibrium with the rock would promote the precipitation of carbonate, and phyllosilicate minerals, resulting in a time-dependent decrease in permeability and sealing. Coseismic increases in permeability may also facilitate up-dip migration of hotter fault zone fluids into the alteration zone [*Sibson*, 1992; *Menzies et al*., 2016]. The net effect of enhanced fluid migration within the alteration zone is the gradual reduction in porosity and permeability within these materials through a combination of

Figure 11. Plate boundary cross section and schematic model of earthquake cycle processes occurring on the Alpine Fault at Gaunt Creek. (a) There are several fluid sources within the Alpine Fault Zone, including mantle (green arrows) and metamorphic (yellow arrows) fluids, but meteoric water (blue arrows) is volumetrically dominant within the brittle crust (modified from *Menzies et al*. [2016]). (b–d) Diagrams illustrating key processes that affect fault core permeability and, potentially, rheology. The Alpine Fault forms an impermeable barrier throughout the earthquake cycle (bold diagonal line). (b) Immediately after an earthquake, hanging wall and footwall permeability is relatively high due to off-fault fractures (i.e., damage). Damage is likely greater in the hanging wall [e.g., *Ma and Beroza*, 2008]. Short black lines denote open fractures; open purple circles represent phyllosilicates. (c) As meteoric fluids pond against the impermeable fault, carbonate (calcite) precipitates and seals open fractures during the interseismic period. The footwall is isolated from calcite-rich meteoric fluids. Short magenta lines denote calcite-sealed fractures. (d) During the late-interseismic period, open fractures near the Alpine Fault are sealed with calcite. Phyllosilicate nucleation and growth occurs more slowly; phyllosilicates within the fault core likely formed over multiple earthquake cycles [e.g., *Meunier*, 2005].

grain-scale healing and fracture sealing through precipitation (which requires advective fluid flow and infiltration) [e.g., *Warr and Cox*, 2001; *Townend et al*., 2013]. Thus, fault strength increases, and permeability decreases, during the interseismic phase of the earthquake cycle (Figure 11).

A limitation of this qualitative model, derived from data on surface-outcrop fault rocks and supported by results from the shallow DFDP-1 boreholes, is that it does not address lithological, spatial, and temporal variations in fault zone healing rates. Within framework silicate-rich fault core gouges, compaction and frictional strengthening via solution-assisted mass transfer processes occur most rapidly at temperatures $\geq$150°C on short-time scales (days–weeks or months) [*Renard et al*., 2000; *Niemeijer et al*., 2002; *Tenthorey and Cox*, 2006; *Gratier et al*., 2009]. However, the healing mechanism in phyllosilicate-rich gouges, such as those described here in DFDP-1A and 1B, is poorly understood. In the San Andreas Fault Observatory at Depth (SAFOD), for example, trioctahedral smectite (saponite)-rich gouges are actively creeping [e.g., *Holdsworth et al*., 2011]. Laboratory experiments on fault gouge analogues indicate that phyllosilicate-rich gouges do not heal via solid-state or solution-assisted mass transfer [e.g., *Dieterich*, 1978; *Bos and Spiers*, 2000; *Niemeijer and Spiers*, 2006]. Products of alteration reactions observed in the smectite-bearing Unit 5 gouges present in DFDP-1A and 1B, as well as other localities along strike of the fault, include calcite and iron hydroxide (Tables 3 and 4, Figure 4g). Porosity reduction via precipitation of these minerals as cement may be influential in sealing the fault core gouges in the upper ~2 km of the fault (Figure 11).

Permeability changes in strike-slip fault zones as a function of gouge compaction, crack sealing, and fluid flow from depth have been modeled quantitatively [*Gratier et al*., 2003; *Gratier and Gueydan*, 2007]. According to these models, late interseismic lithostatic pore fluid overpressures develop most quickly at two different depth intervals: in the upper crust (30°C<T<90°C) where calcite is available for mass transfer and relatively fast sealing of veins, and at depth (150°C<T<300°C) due to increased quartz solubility combined with inflow of fluids from the lower crust. In turn, depth-dependent lithostatic pore fluid pressures develop within 270 years following an earthquake [*Gratier and Gueydan*, 2007]. Although these models depend critically on the kinetics of the involved dissolution and precipitation reactions as well as on diffusion rates, 270 years is within the recurrence interval of Alpine Fault earthquakes (329 $\pm$ 68 years) [*Berryman et al*., 2012].

Abundant evidence exists for persistent 100 m to 1 km-thick damage zones in the shallow crust (<3 km) [e.g., *Chester and Logan*, 1986; *Li et al*., 1990, 2000, 2004; *Mitchell and Faulkner*, 2009; *Yang et al*., 2011]. However, within the fault core-alteration zone at Gaunt Creek, and elsewhere along the Alpine Fault, hanging wall fractures have been sealed by authigenic precipitation of calcite and phyllosilicates [*Sutherland et al*., 2012; *Townend et al*., 2013] (Table 3) (Figures 5c, 5f, and 7–9). This sealing has decreased fault normal permeability and increased rock mass competency, potentially promoting interseismic strain buildup (Figure 11). Further research aimed toward understanding mass transfer processes within the fault zone is integral to underpinning the mechanisms responsible for variations in late interseismic fault zone strength [e.g., *Finzi et al*., 2011].

To quantify the physical processes driving the seismic cycle on the Alpine Fault, better constraints on mineral reactions, reaction rates, diffusion rates, compaction, and healing rates in the laboratory and in naturally deformed fault rocks are needed [e.g., *Renard et al*., 2000, 2012; *Gratier et al*., 2003]. In addition, geophysical and geochemical observations of fluid flux during interseismic, coseismic, and postseismic periods are needed for numerical models that quantify how fluid migration, porosity, permeability, and rock strength evolve at depth and during exhumation [*Menzies et al*., 2016]. Incorporating permeability and fluid pressure evolution variables into empirical rate and state-dependent constitutive laws will ultimately better constrain how fluid-rock interactions influence fault strength evolution, strain accumulation, and the timing and mode of earthquake rupture nucleation [e.g., *Sibson*, 1992; *Segall and Rice*, 1995; *Sibson and Rowland*, 2003; *Hillers and Miller*, 2007, *Ben-Zion*, 2008; *Samuelson et al*., 2009].

6. Conclusions

1. On the Alpine Fault at Gaunt Creek, a fault core extends into the hanging wall up to ~20–30 m from the PSZ assuming that the first documented occurrence of retrogressed mineral assemblages in the Unit 2 brown-green-black ultramylonites represents the maximum extent of alteration zone processes within the fault core.

2. The presence of the low-temperature clay minerals montmorillonite and kaolinite, along with the high measured LOI values, in the brown smectite-bearing Unit 5 PSZ gouges suggests that these units are the most highly altered rocks recovered. The presence of variably comminuted vein calcite and secondary calcite cement is reflected in the major element geochemistry of the PSZ gouges, where CaO concentrations are higher than in adjacent Unit 6 lower cataclasites.
3. Similar montmorillonite-bearing Unit 5 PSZ gouges were collected from thrust segments of the central Alpine Fault at Little Man River, Waikukupa River, and Robinson Creek, an along-strike distance of 120 km. These field observations delimit the minimum near-surface extent of principal slip zone materials recovered during DFDP-1.
4. Minerals, microstructures, and major elements measured in the DFDP-1 fault rocks reflect seismic cycle processes. Within the alteration zone, off-fault damage has created brittle fractures that facilitate the infiltration of meteoric and (potentially) metamorphic or rock-exchanged hydrothermal fluids. These fluids promote carbonate and phyllosilicates precipitation, which in turn gradually decrease porosity and permeability through a combination of grain-scale healing and fracture sealing (e.g., Table 7, Figures 3−6 and 11).
5. Interseismic increases in fault strength promoted by fluid-rock interactions allow the Alpine Fault to accumulate the stored elastic strain energy necessary for earthquake rupture nucleation and propagation [e.g., *Kanamori and Brodsky*, 2001].

Acknowledgements
The following people, companies, and institutions made the Deep Fault Drilling Project (DFDP-1) successful: Horizon Drilling, Alex Pyne, the New Zealand Department of Conservation, the Marsden Fund, GNS Science, Victoria University of Wellington and the Universities of Otago, Auckland, Canterbury, Liverpool, and Bremen. The first author would like to thank Mark Raven, Brent Pooley, Damian Walls, and Carmel Pinnington for excellent technical assistance. The manuscript benefited greatly from reviews by Jim Evans and an anonymous reviewer. All data are located in supporting information. C.B. and C.D.M. are supported by NERC grant NE/J02449/1.

References

Allis, R., and Y. Shi (1995), New insights into temperature and pressure beneath the central Southern Alps, New Zealand, *N. Z. J. Geol. Geophys.*, *38*, 585–592.
Ague, J. J. (1994), Mass transfer during Barrovian metamorphism of pelites, south-central Conneticut. I: Evidence for changes in composition and volume, *Am. J. Sci.*, *294*, 989–1057.
Barnes, I., C. Downes, and J. Hurlston (1978), Warm springs, South Island New Zealand, and their potentials to yield laumontite, *A. J. Sci.*, *278*(1), 1412–1427.
Barth, N. C., V. Toy, R. Langridge, and R. Norris (2012), Scale dependence of oblique plate-boundary partitioning: New insights from LiDAR, central Alpine fault, New Zealand, *Lithosphere*, *4*, 435–448, doi:10.1130/L201.1.
Barth N. C., C. Boulton, B. M. Carpenter, G. E. Batt, and V. G. Toy (2013), Slip localization on the southern Alpine Fault, New Zealand, *Tectonics*, *32*, 620–640, doi:10.1002/tect.20041.
Batt G., S. Baldwin, M. Cottam, P. Fitzgerald, M. Brandon, and T. Spell (2004), Cenozoic plate boundary evolution in the South Island of New Zealand: New thermochronological constraints, *Tectonics*, *23*, TC4001, doi:10.1029/2003TC001527.
Beavan J., et al. (1999), Crustal deformation during 1994-1998, due to oblique continental collision in the central Southern Alps, New Zealand, and implications for seismic potential of the Alpine fault, *J. Geophys. Res.*, *104*(B11), 25,233–25,255, doi:10.1029/1999JB900198.
Beavan, J., Denys, P., Denham, M., Hager, B., Herring, T. and P. Molnar (2010), Distribution of present-day vertical deformation across the Southern Alps, New Zealand, from 10 years of GPS data, *Geophs. Res. Lett.*, *37*, L16305, doi:10.1029/2010GL044165.
Ben-Zion, Y. (2008), Collective behavior of earthquakes and faults: Continuum-discrete transitions, progressive evolutionary changes, and different dynamic regimes, *Rev. Geophys.*, *46*, RG4006, doi:10.1029/2008RG000260.
Berryman, K., S. Beanland, A. Cooper, H. Cutten, R. Norris, and P. Wood (1992), The Alpine Fault, New Zealand: Variation in Quaternary structural style and geomorphic expression. *Ann. Tectonicae*, *IV*, 126–163.
Berryman, K.B., U.A. Cochran, K.J. Clark, G.P. Biasi, R.M. Langridge, and P. Villamor (2012), Major earthquakes occur regularly on an isolated plate boundary fault, *Science*, *29*(336), 1690–1693, doi:10.1126/science.1218959.
Bos, B., and C. J. Spiers (2000), Effect of phyllosilicates on fluid-assisted healing of gouge-bearing faults, *E. Planet. Sci. Lett.*, *184*, 199–210.
Bos, B., and C. J. Spiers (2001), Experimental investigation into the microstructural and mechanical evolution of phyllosilicate-bearing fault rock under conditions favouring pressure solution, *J. Struct. Geol.*, *23*, 1187–1202.
Bos, B., and C. J. Spiers (2002), Frictional-viscous flow of phyllosilicate-bearing fault rock: Microphysical model and implications for crustal strength profiles, *J. Geophys. Res.*, *107*(B2), 2028, doi:10.1029/2001JB000301.
Boulton, C., B. M. Carpenter, V. Toy, and C. Marone (2012), Physical properties of surface outcrop cataclastic fault rocks, Alpine Fault, New Zealand, *Geochem. Geophys. Geosyst.*, *13*, Q01018, doi:10.1029/2011GC003872.
Boulton, C., D. Moore, D. Lockner, V. Toy, J. Townend, and R. Sutherland (2014), Frictional strength and stability of exhumed fault gouges in DFDP-1 cores, Alpine Fault, New Zealand, *Geophys. Res. Lett.*, *41*, 356–362, doi:10.1002/2013GL058236.
Caine, J., J. Evans, and C. Forster (1996), Fault zone architecture and permeability structure. *Geology*, *24*(11), 1025–1028.
Cande, S. C., and J. M. Stock (2004), Pacific-Antarctic-Australia motion and the formation of the Macquarie Plate, *Geophys. J.*, *157*, 399–414.
Carpenter, B. M., H. Kitajima, and D. M. Saffer (2014), Permeability and elastic properties of the active Alpine Fault, New Zealand: Measurements on DFDP-1 drill core, *Earth Planet. Sci. Lett.*, *390*, 45–51, doi:10.1016/j.epsl.2013.12.023.
Carter, R. M., and R. J. Norris (1976), Cainozoic history of southern New Zealand: An accord between geological observations and plate tectonic predictions, *Earth Planet. Sci. Lett.*, *31*, 85–94.
Chamberlain, C., M. Poage, D. Craw, and R. Reynolds (1999) Topographic development of the Southern Alps recorded by the isotopic composition of authigenic clay minerals, South Island, New Zealand, *Chem. Geol.*, *155*, 279–294.
Chen, J., X. Yang, S. Ma, and C.J. Spiers (2013), Mass removal and clay mineral dehydration/rehydration in carbonate-rich surface exposures of the 2008 Wenchuan Earthquake fault: Geochemical evidence and implications for fault zone evolution and coseismic slip, *J. Geophys. Res. Solid Earth*, *118*, 474–496, doi:10.1002/jgrb50089.
Chester, F., and J. Chester (1998), Ultracataclasite structure and friction processes of the Punchbowl fault, San Andreas system, California, *Tectonophysics*, *295*, 199–221.
Chester, F., and N. Higgs (1992), Multimechanism friction constitutive model for ultrafine quartz gouge at hypocentral conditions, *J. Geophys. Res.*, *97*(B2), 1859–1870.

Chester, F. M., and J. M. Logan (1986), Implications for mechanical properties of brittle faults from observations of the Punchbowl fault zone, California, *Pure Appl. Geophys.*, *124*, 79–106.
Chester, F. M., J. P. Evans, and R. L. Biegel (1993), Internal structure and weakening mechanisms of the San Andreas fault, *J. Geophys. Res.*, *98*(B1), 771–786.
Collettini, C., and R. E. Holdsworth (2004), Fault zone weakening and character of slip along low-angle normal faults: Insights from the Zuccale fault, Elba, Italy, *J. Geol. Soc. London*, *161*, 1039–1051.
Collettini, C., Niemeijer, A., Viti, C., and C. Marone (2009), Fault zone fabric and fault weakness, *Nature*, *462*, 907–910, doi:10.1038/nature08585.
Cooper, A. F., and R. J. Norris (1994), Anatomy, structural evolution and slip rate of a plate-boundary thrust: The Alpine fault at Gaunt Creek, Westland, New Zealand, *Geol. Soc. Am. Bull.*, *106*, 627–633.
Cooper, A. F., and R. J. Norris (2011), Inverted metamorphic sequences in Alpine fault mylonites produced by oblique shear within a plate boundary fault zone, New Zealand, *Geology*, *39*(11), 1023–1026. doi:10.1130/G32273.
Craw, D. (1988), Shallow level penetration of metamorphic fluids in a high uplift rate mountain belt, Southern Alps, New Zealand, *J. Metamorph. Geol.*, *6*, 1–16.
Craw, D., and J. R. Campbell (2004), Tectonic and structural setting for active mesothermal gold vein systems, Southern Alps, New Zealand, *J. Struct. Geol.*, *26*, 995–1005.
Deer, W. A., R. A. Howie, and J. Zussman (1992), *An Introduction to Rock-Forming Minerals*, 2nd ed., Longman, Essex.
De Pascale, G. P., and R. M. Langridge (2012), New on-fault evidence for a great earthquake in A.D. 1717, central Alpine fault, New Zealand, *Geology*, *40*(9), 791–794, doi:10.1130/G33363.1.
Dieterich, J. (1978), Time-dependent friction and the mechanics of stick-slip, *Pure App. Geophys.*, *116*, 790–805.
Easterbrook, L. (2010), The Alpine Fault Zone Along the Waitangi-taona River, West Coast, New Zealand, MSc thesis, University of Otago, Dunedin.
Evans, J. P., and F. M. Chester (1995), Fluid-rock interaction in faults of the San Andreas system: Inferences from San Gabriel fault rock geochemistry and microstructures, *J. Geophys. Res.*, *100*(B7), 13,007–13,020.
Evison, F. (1971), Seismicity of the Alpine Fault, New Zealand. Recent Crustal Movements, *Bull. R. Soc. N. Z.*, *9*, 161–165.
Finzi, Y., E. H. Hearn, V. Lyakhovsky, and L. Gross (2011), Fault-zone healing effectiveness and the structural evolution of strike-slip fault systems, *Geophys. J. Int.*, *186*, 963–970.
Gaina, C., D. R. Mueller, J.-Y. Royer, J. Stock, J. Hardebeck, and P. Symonds (1998), The tectonic history of the Tasman Sea: A puzzle with 13 pieces, *J. Geophys. Res.*, *103*(6), 12,413–12,433, doi:10.1029/98JB00386.
Garagash, D. (2012), Seismic and aseismic slip pulses driven by thermal pressurization of pore fluid, *J. Geophys. Res.*, *117*, B04314, doi:10.1029/2011JB008889.
Goddard, J. V., and J. P. Evans (1995), Chemical changes and fluid-rock interaction in fault of crystalline thrust sheets, northwestern Wyoming, U.S.A, *J. Struct. Geol.*, *17*, 533–547.
Grant, J. A. (1986), The isocon diagram; a simple solution to Gresens' equation for metasomatic alteration, *Econ. Geol.*, *81*, 1976–1982.
Gratier, J-P., P. Favreau, and F. Renard (2003), Modeling fluid transfer along California faults when integrating pressure solution crack sealing and compaction processes, *J. Geophys. Res.*, *108*(B2), 2104, doi:10.1029/2001JB000380.
Gratier, J-P., and F. Gueydan (2007), Deformation in the presence of fluids and mineral reactions: effect of fracturing and fluid-rock interaction on seismic cycles, in *Tectonic Faults: Agents of Change on a Dynamic Earth*, edited by M. R. Handy, G. Hirth, and N. Hovius, pp. 319–356, The MIT Press, Cambridge, Mass.
Gratier, J-P., R. Guiguet, F. Renard, L. Jenatton, and D. Bernard (2009), A pressure solution creep law for quartz from identation experiments, *J. Geophys. Res.*, *114*(B03403), doi:10.1029/2008JB005652.
Gresens, R. L. (1967), Composition-volume relationships of metasomatism. *Chem. Geol.*, *2*, 47–65.
Hickman, S., R. Sibson, and R. Bruhn (1995), Introduction to special section: Mechanical involvement of fluids in faulting. *J. Geophys. Res.*, *100*(B7), 12,831–12,840.
Hillers, G., and S. Miller (2007), Dilatancy controlled spatiotemporal slip evolution of a sealed fault with spatial variations of the pore pressure, *Geophys. J. Int.* , *168*, 431–445, doi:10.1111/j.1365-246X.2006.03167.
Holdsworth, R. E., E. W. E. van Diggelen, C. J. Spiers, J. H. P. de Bresser, R. J. Walker, and L. Bowen (2011), Fault rocks from the SAFOD core samples: Implications for weakening at shallow depths along the San Andreas Fault, California, *J. Struct. Geol.*, *33*, 132–144.
Holland, T. J. B., and R. Powell (1998), An internally consistent thermodynamic data set for phases of petrological interest, *J. Metamorph. Geol.*, *16*, 309–343.
Howarth, J. D., S. J. Fitzsimmons, R. J. Norris, G. E. Jacobsen (2012), Lake sediments record cycles of sediment flux driven by large earthquakes on the Alpine fault, New Zealand, *Geology*, *40*, 1091–1094, doi:10.1130/G33486.1.
Isaacs, A. J., J. P. Evans, P. T. Kolesar, and T. Nohara (2008), Composition, microstructures, and petrophysics of the Mozumi fault, Japan: In situ analyses of fault zone properties and structure in sedimentary rocks from shallow crustal levels, *J. Geophys. Res.*, *113*, B12408, doi:10.1029/2007JB005314.
Janecke, S. U., and J. P. Evans (1988), Feldspar-influenced rock rheologies, *Geology*, *16*(12), 1064–1067.
Jefferies, S. P., R. E. Holdsworth, T. Shimamoto, H. Takagi, G. E. Lloyd, and C. J. Spiers (2006), Origin and mechanical significance of foliated cataclastic rocks in the cores of crustal-scale faults: Examples from the Median Tectonic Line, Japan, *J. Geophys. Res.*, *111*(B12303), doi:10.1029/2005JB004205
Kanamori, H., and E. E. Brodsky (2001), The Physics of Earthquakes, *Phys. Today*, *54*, doi:10.1063/1.1387590.
King, G. C. P. (1986), Speculations on the geometry of the initiation and termination processes of earthquake rupture and its relation to morphology and geological structure. *Pure Appl. Geophys.*, *124*, 567–585.
Koons, P. O., and D. Craw (1991), Evolution of fluid driving forces and composition within collisional orogens, *Geophys. Res. Lett.*, *18*, 935–938, doi:10.1029/91GL00910.
Koons, P. O., D. Craw, S. Cox, P. Upton, A. S. Templeton, and C. P. Chamberlain (1998), Fluid flow during oblique convergence: A Southern Alps model from mechanical and geochemical observations, *Geology*, *26*(2), 159–162.
Lamb, S., and E. Smith (2013), The nature of the plate interface and driving force of interseismic deformation in the New Zealand plate-boundary zone, revealed by the continuous GPS velocity field, *J. Geophys. Res. Solid Earth*, *118*, 3160–3189, doi:10.1002/jgrb.50221.
Lamb, S., E. Smith, T. Stern, and E. Warren-Smith (2015), Continent-scale strike-slip on a low-angle fault beneath New Zealand's Southern Alps: Implications for crustal thickening in oblique collision zones, *Geochem., Geophys., Geosyst.*, *16*, 3076–3096, doi:10.1002/2015GC005990.

Lamb, S., N. Mortimer, E. Smith, and G. Turner (2016), Focusing of relative plate motion at a continental transform fault: Cenozoic dextral displacement >700 km on New Zealand's Alpine Fault, reversing >225 km of Late Cretaceous sinistral motion. *Geochem., Geophys., Geosyst.*, *17*, 1197–1213, doi:10.1002/2015GC006225.
Landis, C. A., and D. S. Coombs (1966), Metamorphic belts and orogenesis in southern New Zealand, *Tectonophysics*, *4*, 501–518.
Li, Y. G., P. G. Leary, K. Aki, and P. Malin (1990), Seismic trapped modes in the Oroville and San Andreas fault zones, *Science*, *249*, 763–766.
Li, Y. G., J. E. Vidale, K. Aki, and F. Xu, (2000), Depth-dependent structure of the Landers fault zone using fault zone trapped waves generated by aftershocks, *J. Geophys. Res.*, *105*(B3), 6237–6254.
Li, Y. G., J. R. Vidale, and E. Cochran (2004), Low-velocity damaged structure of the San Andreas Fault at Parkfield from fault zone trapped waves, *Geophys. Res. Lett.*, *31*, L12S06, doi:10.1029/2003GL019044.
Little, T. A., Cox, S., Vry, J. K., and G. Batt (2005), Variations in exhumation level and uplift-rate along the oblique-slip Alpine fault, central Southern Alps, New Zealand, *Geol. Soc. Am. Bull.*, *117*(5-6), 707–723.
Ma, S., and G. C. Beroza (2008), Rupture dynamics on a biomaterial interface for dipping for dipping faults *Bull. Seismol. Soc. Am.*, *98*(4), 1642–1658.
McClintock, M. K. (1999), Alpine Fault Zone structure and tectonometamorphic evolution, Makawhio River, South Westland, BSc (Hons) thesis,University of Otago, Dunedin.
McClintock, M. K., and A. F. Cooper (2003), Geochemistry, mineralogy, and metamorphic history of kyanite-orthoamphibole-bearing Alpine Fault mylonite, South Westland, New Zealand, *N. Z. J. Geol. Geophys.*, *46*, 47–62, doi:10.1080/00288306.2003.9514995.
Menzies, C. D., D. A. H. Teagle, D. Craw, S. C. Cox, A. J. Boyce, and D. Barrie (2014), Incursion of meteoric waters into the ductile regime in an active orogeny, *Earth Planet. Sci. Lett.*, *399*, 1–14.
Menzies, C. D., D. A. H. Teagle, S. Niedermann, S. C. Cox, D. Craw, M. Zimmer, M. J. Cooper, and J. Erzinger (2016), The fluid budget of a continental plate boundary fault: Quantification from the Alpine Fault, New Zealand, *Earth Planet. Sci. Lett.*, *445*, 125–135, doi:10.1016/j/epsl.2016.03.046.
Mitchell, T. M., and D. R. Faulkner (2009), The nature and origin of off-fault damage surrounding strike-slip fault zones with a wide range of displacements: A field study from the Atacama fault system, northern Chile, *J. Struct. Geol.*, *31*, 802–816.
Mizoguchi, K., and K. Ueta (2013), Microfractures within the fault damage zone record the history of fault activity, *Geophys. Res. Lett.*, *40*, 2023–2027, doi:10.1002/grl50469.
Molnar, P., T. Atwater, J. Mammerickx, and S.M. Smith (1975), Magnetic anomalies, bathymetry and the tectonic evolution of the South Pacific since the Late Cretaceous, *Geophys. J. Int.*, *40*(3), 383–420.
Moore, D. E., and D. A. Lockner (2004), Crystallographic controls on the frictional behavior of dry and water-saturated sheet structure minerals, *J. Geophys. Res.*, *109*, B03401, doi:10.1029/2003JB002582.
Mortimer, N. (2004), New Zealand's geological foundations. *Gondwana Res.*, *7*, 261–272.
Meunier, A. (2005), *Clays*, 472 pp., Springer, Berlin.
Nathan, S. (1976), Geochemistry of the Greenland Group (Early Ordovician), New Zealand, *N. Z. J. Geol. Geophys*, *19*, 683–706.
Niemeijer, A., and C. J. Spiers (2005), Influence of phyllosilicates on fault strength in the brittle-ductile transition: Insights from rock analogue experiments, *Geol. Soc. Spec. Publ.*, *245*, 303–327.
Niemeijer, A. R., and C. J. Spiers (2006), Velocity dependence of strength and healing behavior in simulated phyllosilicate-bearing fault gouge, *Tectonophys.*, *427*, 231–253.
Niemeijer, A. R., C. Boulton, V. G. Toy, J. Townend, and R. Sutherland (2016), Large-displacement, hydrothermal frictional properties of DFDP-1 fault rocks, Alpine Fault, New Zealand: Implications for deep rupture propagation, *J. Geophys. Res. Solid Earth*, *121*, 624–647, doi:10.1002/2015JB012593.
Niemeijer, A. R., C. J. Spiers, and B. Bos (2002), Compaction creep of quartz sand at 400-600°C: experimental evidence for dissolution-controlled pressure solution, *E. Planet. Sci. Lett.*, *195*, 261–275.
Norris, R. J., and A. F. Cooper (2007), The Alpine Fault, New Zealand: Surface geology and field relationships, in *A Continental Plate Boundary: Tectonics at South Island, New Zealand, Geophys. Monogr. Ser.*, vol. 175, edited by D. Okaya, T. Stern, and F. Davey, pp. 159–178, AGU, Washington, D. C., doi:10.1029/175GM09.
O'Hara, K. (1988), Fluid flow and volume loss during mylonitization: An origin for phyllonite in an overthrust setting, North Carolina, USA, *Tectonophysics*, *156*, 21–36.
Pitcairn, I. K. (2004), Sources of fluids and metals in orogenic gold deposits: The Otago schist's, New Zealand, PhD thesis, University of Southampton, Southampton, U. K.
Pitcairn, I. K., D. A. H. Teagle, D. Craw, G. R. Olivo, R. Kerrich, and T. S. Brewer (2006), Sources of metals and fluids in orogenic gold deposits: Insights from the Otago and Alpine Schists, New Zealand, *Econ. Geol.*, *101*, 1525–1546.
Platt, J. D., R. C. Viesca, and D. I. Garagash (2015), Steadily propagating slip pulses driven by thermal decomposition, *J. Geophys. Res. Solid Earth*, *120*, 6558–6591, doi:10.1002/2015JB012200.
Prior, D. J. (1988), Deformation processes in the Alpine Fault Mylonites, South Island, New Zealand, PhD thesis, University of Leeds, Leeds, U. K.
Reed, J. J. (1964), Mylonites, cataclasites, and associated rocks along the Alpine Fault, South Island, New Zealand, *N. Z. J. Geol. Geophys*, *7*, 645–684.
Renard, F., J. Gratier, and B. Jamtveit (2000), Kinetics of crack-sealing, intergranular pressure solution, and compaction around active faults, *J. Struct. Geol.*, *22*, 1395–1407.
Renard, F., S. Beaupretre, C. Voisin, D. Zigone, T. Candela, D.K. Dysthe, and J-P. Gratier (2012), Strength evolution of a reactive frictional interface is controlled by the dynamics of contacts and chemical effects, *Earth Planet. Sci. Lett.*, *341-344*, 20–34.
Roser, B. P., and A. F. Cooper (1990), Geochemistry and terrane affiliation of Haast Schist from the western Southern Alps, New Zealand, *N. Z. J. Geol. Geophys.*, *33*(1), 1–10.
Roser, B. P., and R. J. Korsch (1999), Geochemical characterization, evolution and source of a Mesozoic accretionary wedge: The Torlesse terrane, New Zealand, *Geol. Mag.*, *136*, 493–512.
Roser, B. P., R. H. Grapes, and K. Palmer (1995), XRF analyses of sandstones and argillites from the Torlesse terrane, New Zealand, *Geol. Board Stud. Publ.*, vol. 15, 40 pp., Res. Sch. of Earth Sci., Victoria University, Wellington.
Rowe, C. D., F. Meneghini, and J. Casey Moore (2011), Textural record of the seismic cycle: Strain-rate variation in an ancient subduction thrust, in *Geology of the Earthquake Source: A Volume in Honour of Rick Sibson, Geol. Soc. London Spec. Pub.*, vol. 359, edited by Fagereng A., V. G. Toy, and J. V. Rowland, pp. 77–95, Geol. Soc. London, London.
Samuelson, J., D. Elsworth, and C. Marone (2009), Shear-induced dilatancy of fluid-saturated faults: Experiment and theory, *J. Geophys. Res.*, *114*, B12404, doi:10.1029/2008JB006273.
Schleicher, A. M., S. N. Tourscher, B. A. van der Pluijm, and L. N. Warr (2009), Constraints on mineralization, fluid-rock interaction, and mass transfer during faulting at 2-3 km depth from the SAFOD drill hole, *J. Geophys. Res.*, *114*, B04202, doi:10.1029/2008JB006092.

Schleicher, A. M., R. Sutherland, J. Townend, V. G. Toy, and B. A. van der Pluijm (2015), Clay mineral formation and fabric development in the DFDP-1B borehole, central Alpine Fault, New Zealand, *N. Z. J. Geol. Geophys.*, *58*(1), 13–21, doi:10.1080/00288306.2014.979841.
Scholz, C. H. (2002). *The Mechanics of Earthquakes and Faulting*, 2nd ed., Cambridge Univ. Press, New York.
Schulz, S. E., and J. P. Evans (1998), Spatial variability in microscopic deformation and composition of the Punchbowl fault, Southern California: Implications for mechanisms, fluid-rock interaction, and fault morphology, *Tectonophysics*, *295*, 223–244, doi:10.1016/S0040-1951(98)00122-X.
Schulz, S. E., and J. P. Evans (2000), Mesoscopic structure of the Punchbowl fault, southern California, and the geologic and geophysical structure of active strike-slip faults, *J. Struct. Geol.*, *22*, 913–930, doi:10.1016/S0191-8141(00)00019-5.
Scott, H. R. (2012), Cataclastic processes within the Alpine fault zone, MSc thesis, University of Otago, Dunedin.
Segall, P., and J. R. Rice (1995), Dilatancy, compaction, and slip instability of a fluid-infiltrated fault, *J. Geophys. Res.*, *100*(B11), 22,155–22,171, doi:10.1029/95JB02403.
Sibson, R. H. (1977), Fault rocks and fault mechanisms, *Geol. Soc. London J.*, *133*, 191–213.
Sibson, R. H. (1982), Fault zone models, heat flow, and the depth distribution of earthquakes in the continental crust of the United States, *Bull. Seismol. Soc. Am.*, *72*(1), 151–163.
Sibson, R. H. (1991), Loading of faults to failure. *Bull. Seismol. Soc. Am.*, *81*(6), 2493–2497.
Sibson, R. H. (1992), Implications of fault-valve behaviour for rupture nucleation and recurrence, *Tectonophysics*, *211*, 283–293.
Sibson, R. H. (2003), Thickness of the seismic slip zone. *Bull. Seismol. Soc. Am.*, *93*, 1169–1178, doi:10.1785/0120020061.
Sibson, R. H., and J. V. Rowland (2003), Stress, fluid pressure and structural permeability in seismogenic crust, North Island, New Zealand, *Geophys. J.*, *154*, 584–594.
Sibson, R. H, S. H. White, and B. K. Atkinson (1979), Fault rock distribution and structure within the Alpine Fault Zone: A preliminary account, *Bull. R. Soc. N. Z.*, *18*, 55–65.
Simpson, G. D. H. (1992), Quaternary evolution of the Alpine Fault Zone, and a mineralogical/microstructural study of the schist-mylonite transition, BSc (Hons) thesis, University of Otago, Dunedin.
Simpson, G. D. H., A. F. Cooper, and R. J. Norris (1994), Late Quaternary evolution of the Alpine Fault Zone at Paringa, South Westland, New Zealand, *N. Z. J. Geol. Geophys*, *37*, 49–58.
Sleep, N. H., and M. L. Blanpied (1992), Creep, compaction, and the weak rheology of major faults, *Nature*, *359*, 687–692.
Smith, S. A. F., R. E. Holdsworth, C. Collettini, and M. A. Pearce (2011), The microstructural character and mechanical significance of fault rocks associated with a continental low-angle normal fault: The Zuccale Fault, Elba Island, Italy, in *Geology of the Earthquake Source: A Volume in Honour of Rick Sibson, Geol. Soc. London Spec. Pub.*, vol. 359, edited by A. Fagereng, V. G. Toy, and J. V. Rowland, pp. 97–113, Geol. Soc. London, London, U. K.
Sutherland, R. (1995), The Australia-Pacific boundary and Cenozoic plate motions in the SW Pacific; some constraints from Geosat data, *Tectonics*, *14*(4), 819–831.
Sutherland, R. (1999), Basement geology and tectonic development of the greater New Zealand region: An interpretation from regional magnetic data, *Tectonophys.*, *308*(3), 341–362, doi:10.1016/S0040-1951(99)00108-0.
Sutherland, R., F. Davey, and J. P. Beavan (2000), Plate boundary deformation in South Island, New Zealand, is related to inherited lithospheric structure, *Earth Planet. Sci. Lett.*, *177*, 141–151.
Sutherland, R., et al. (2007), Do great earthquakes occur on the Alpine fault in central South Island, New Zealand?, in *A Continental Plate Boundary: Tectonics at South Island, New Zealand, Geophys. Monogr. Ser.*, vol. 175, edited by D. Okaya et al., pp. 235–251, AGU, Washington, D. C.
Sutherland, R., et al. (2011), Operations and well completion report for boreholes DFDP-1A and DFDP-1B, Deep Fault Drilling Project, Alpine Fault, Gaunt Creek, New Zealand, *GNS Sci. Rep., 2011/48*, 70 p., Inst. of Geol. & Nuclear Sciences, Lower Hutt, N. Z.
Sutherland, R., et al. (2012), Drilling reveals fluid control on architecture and rupture of the Alpine Fault, New Zealand, *Geology*, *40*, 1143–1146, doi:10.1130/G33614.1.
Tanikawa, W., H. Mukoyoshi, O. Tadai, T. Hirose, A. Tsutsumi, and W. Lin (2012), Velocity dependence of shear-induced permeability associated with frictional behavior in fault zones of the Nankai subduction zone, *J. Geophys. Res.*, *117*, B05405, doi:10.1029/2011JB008956.
Tembe, S., D. A. Lockner, and T. F. Wong (2010), Effect of clay content and mineraology on frictional sliding behavior of simulated gouges: Binary and ternary mixtures of quartz, illite, and montmorillonite, *J. Geophys. Res.*, *115*, B03416, doi:10.1029/2009JB006383.
Templeton, A. S., C. P. Chamberlain, P. O. Koons, and D. Craw (1998), Stable isotopic evidence for mixing between metamorphic fluids and surface-derived waters during recent uplift of the Southern Alps, New Zealand, *E. Planet. Sci. Lett.*, *154*, 73–92.
Tenthorey, E., and S. Cox (2006), Cohesive strengthening of fault zones during the interseismic period: an experimental study, *J. Geophys. Res. Solid Earth*, *111*(B9), doi:10.1029/2005JB004122.
Totten, M. W., M. A. Hanan, D. Knight, and J. Borges (2002), Characteristics of mixed-layer smectite/illite density separates during burial diagenesis, *Am. Mineral*, *87*(11-12), 1571–1579, doi:10.2138/am-2002-11-1207.
Townend, J., R. Sutherland, V. G. Toy, J. D. Eccles, C. J. Boulton, S. C. Cox, and D. McNamara (2013), Late-interseismic state of a continental plate-bounding fault: Petrophysical results from DFDP-1 wireline and core analysis, Alpine fault, New Zealand, *Geochem., Geophys., Geosyst.*, *14*, 3801–3820, doi:10.1002/ggge/20236.
Toy, V. G. (2007), Rheology of the Alpine Fault Mylonite Zone: Deformation processes and below the base of the seismogenic zone in a major plate boundary structure, PhD thesis, University of Otago, Dunedin.
Toy, V. G., D. J. Prior, and R. J. Norris (2008), Quartz textures in the Alpine fault mylonites: Influence of pre-existing preferred orientations on fabric development during progressive uplift, *J. Struct. Geol.*, *30*, 602–621.
Toy, V. G., D. Craw, A. F. Cooper, and R. J. Norris (2010), Thermal regime in the central Alpine Fault zone, New Zealand: Constraints from microstructures, biotite chemistry, and fluid inclusion data, *Tectonophysics*, doi:10.1016/j.tecto.2009.12.013.
Toy, V. G., S. Ritchie, and R. H. Sibson (2011), Diverse habitats of pseudotachylytes in the Alpine Fault Zone and relationships to current seismicity, in *Geology of the Earthquake Source: A Volume in Honour of Rick Sibson, Geol. Soc. London Spec. Pub.*, vol. 359, edited by A. Fagereng, V. G. Toy, and J. V. Rowland, pp. 115–133, Geol. Soc. London, London.
Toy, V. G., et al. (2015), Fault rock lithologies and architecture of the central Alpine fault, New Zealand, revealed by DFDP-1 drilling, *Lithosphere*, *7*, 155–173, doi:10.1130/L395
Tulloch, A. J., and K. Palmer (1990), Tectonic implications of granite cobbles from the mid-Cretaceous Pororari Group, southwest Nelson, New Zealand, *N. Z. J. Geol. Geophys*, *33*(2), 205–217.
Tulloch, A. J., J. Ramezani, D. L. Kimbrough, K. Faure, and A. H. Allibone (2009), U-Pb geochronology of mid-Paleozoic plutonism in western New Zealand: Implications for S-type granite generation and growth of the east Gondwana margin, *Geol. Soc. Am. Bull.*, *121*, 1236–1261.
Vry, J., R. Powell, K. M. Golden, and K. Peterson (2009), The role of exhumation in metamorphic dehydration and fluid production, *Nat. Geosci.*, *3*, 31–35.

Upton, P., P. O. Koons, and C. P. Chamberlain (1995), Penetration of deformation-driven meteoric water into ductile rocks: isotopic and model observations from the Southern Alps, New Zealand, *N. Z. J. Geol. Geophys.*, *38*, 535–543.
Vry, J. K., A. C. Storkey, and C. Harris (2001), Role of fluids in the metamorphism of the Alpine Fault Zone, *J. Metamorph. Geol.*, *19*, 21–31.
Walcott, R. I. (1984), Reconstructions of the New Zealand region for the Neogene, *Palaeogeogr., Palaeoclimatol., Palaeoecol.*, *46*, 217–231.
Warr, L. N., and S. Cox (2001), Clay mineral transformations and weakening mechanisms along the Alpine Fault, New Zealand, in *The nature and tectonic significance of fault zone weakening, Geol. Soc. London Spec. Pub.*, vol. 186, edited by R. E. Holdsworth et al., pp. 85–101, Geol. Soc. London, London.
Wellman, H. W. (1953), Data for the study of Recent and late Pleistocene faulting in the South Island of New Zealand, *N. Z. J. Sci. Technol., Sect. B*, *34*, 270–288.
Wells, A, and J. Goff (2007), Coastal dunes in Westland provide a record of paleoseismic activity on the Alpine fault, *Geology*, *35*, 731–734, doi:10.1130/G23554A.1.
Wesnousky, S. G. (1988), Seismological and structural evolution of strike-slip faults, *Nature*, *335*, 340–343.
Wibberley, C. A. J., and T. Shimamoto (2003), Internal structure and permeability of major strike-slip fault zones: The Median Tectonic Line in Mid Prefecture, southwest Japan, *J. Struct. Geol.*, *25*, 59–78.
Wintsch, R. P., and M-W. Yeh (2013), Oscillating brittle and viscous behavior through the earthquake cycle in the Red River Shear Zone: Monitoring flips between reaction and textural softening and hardening, *Tectonophysics*, *587*, 46–62.
Wintsch, R. P., R. Christoffersen, and A. K. Kronenberg (1995), Fluid-rock weakening of fault zones, *J. Geophys. Res.*, *100*(B7), 13,021–13,032, doi:10.1029/1994JB02622.
Woodcock, N. H., and K. Mort (2008), Classification of fault breccias and related fault rocks, *Geol. Mag.*, *145*(3), 434–440.
Wright, C. A. (1998), Geology and Paleoseismology of the Central Alpine Fault New Zealand, MSc thesis, University of Otago, Dunedin.
Yang, H., L. Zhu, and E. S. Cochran (2011), Seismic structures of the Calico fault zone inferred from local earthquake travel time modeling, *Geophys. J.*, *186*, 760–770.